

**Impaired ABCA1/ABCG1-mediated lipid efflux in the mouse retinal pigment epithelium (RPE)
leads to retinal degeneration**

Federica Storti¹, Katrin Klee^{1,2}, Vyara Todorova^{1,3}, Regula Steiner⁴, Alaa Othman⁴, Saskia van der Velde-Visser⁵, Marijana Samardzija¹, Isabelle Meneau⁶, Maya Barben¹, Duygu Karademir^{1,2}, Valda Pauzuolyte¹, Sanford L. Boye⁷, Frank Blaser⁶, Christoph Ullmer⁸, Joshua L. Dunaief⁹, Thorsten Hornemann⁴, Lucia Rohrer⁴, Anneke den Hollander^{5,10}, Arnold von Eckardstein⁴, Jürgen Fingerle¹¹, Cyrille Maugeais⁸ and Christian Grimm^{1,2,3}

¹Lab for Retinal Cell Biology, Department of Ophthalmology, University of Zurich, Schlieren, Switzerland

²Center for Integrative Human Physiology (ZIHP), University of Zurich, Zurich, Switzerland

³Neuroscience Center Zurich (ZNZ), University of Zurich, Zurich, Switzerland

⁴Institute of Clinical Chemistry, University of Zurich, Schlieren, Switzerland

⁵Department of Human Genetics, Radboud University Medical Center, Nijmegen, Netherlands

⁶Department of Ophthalmology, University Hospital Zurich, Zurich, Switzerland

⁷University of Florida, Ophthalmology, Gainesville, FL, USA

⁸Roche Innovation Center Basel, F. Hoffmann-La Roche Ltd, Basel, Switzerland

⁹Department of Ophthalmology, Scheie Eye Institute, University of Pennsylvania, Philadelphia, PA, USA

¹⁰Department of Ophthalmology, Radboud University Medical Center, Nijmegen, Netherlands

¹¹Natural and Medical Sciences Institute, University of Tübingen, Tübingen, Germany

Corresponding author:

Christian Grimm

Lab for Retinal Cell Biology, Department of Ophthalmology, University of Zurich

Wagistrasse 14

CH 8952 Schlieren, Switzerland

Email: cgrimm@opht.uzh.ch

Tel: 0041 44 556 30 01

31 **Abstract**

32 Age-related macular degeneration (AMD) is a progressive disease of the retinal pigment epithelium
33 (RPE) and the retina leading to loss of central vision. Polymorphisms in genes involved in lipid
34 metabolism, including the ATP-binding cassette transporter A1 (*ABCA1*), have been associated with
35 AMD risk. However, the significance of retinal lipid handling for AMD pathogenesis remains elusive.
36 Here, we study the contribution of lipid efflux in the RPE by generating a mouse model lacking *ABCA1*
37 and its partner *ABCG1* specifically in this layer. Mutant mice show lipid accumulation in the RPE,
38 reduced RPE and retinal function, retinal inflammation and RPE/photoreceptor degeneration. Data
39 from human cell lines indicate that the *ABCA1* AMD risk-conferring allele decreases *ABCA1*
40 expression, identifying the potential molecular cause that underlies the genetic risk for AMD. Our
41 results highlight the essential homeostatic role for lipid efflux in the RPE and suggest a pathogenic
42 contribution of reduced *ABCA1* function to AMD.

43 **Most important abbreviations**

44

| | | |
|----|-------|--|
| 45 | ABCA1 | ATP-binding cassette transporter, family A, member 1 |
| 46 | ABCG1 | ATP-binding cassette transporter, family G, member 1 |
| 47 | AMD | Age-related macular degeneration |
| 48 | BEST1 | Bestrophin 1 |
| 49 | CE | Cholesteryl ester |
| 50 | Cer | Ceramide |
| 51 | DAG | Diacylglycerol |
| 52 | GL | Glycerolipid |
| 53 | HDL | High-density lipoprotein |
| 54 | IBA-1 | Ionized calcium-binding adapter molecule 1 |
| 55 | LCL | Lymphoblastoid cell line |
| 56 | LD | Lipid droplet |
| 57 | LXR | Liver X receptor |
| 58 | ONL | Outer nuclear layer |
| 59 | ORO | OilRedO |
| 60 | OS | Outer segment |
| 61 | PL | Phospholipid |
| 62 | RE | Retinyl ester |
| 63 | RHO | Rhodopsin |
| 64 | RPE | Retinal pigment epithelium |
| 65 | SDD | Sub-retinal drusenoid deposit |
| 66 | SL | Sphingolipid |
| 67 | SM | Sphingomyelin |
| 68 | TG | Triglyceride |
| 69 | UC | Un-esterified (free) cholesterol |

Introduction

Age-related macular degeneration (AMD) is the leading cause of blindness in the elderly population of Western countries (Klein et al., 2013; Joachim et al., 2015) and its socio-economic impact is predicted to dramatically increase in the next decades (Wong et al., 2014). AMD is a progressive disease of the macula, the central cone-rich region of the retina, and can develop into the “dry” or “wet” form in the advanced stage. Dry AMD is characterized by atrophy of the retinal pigment epithelium (RPE) and photoreceptor degeneration, while wet AMD exhibits pathological neo-vascularization of the retina originating from the choroid. Both conditions eventually result in loss of RPE and photoreceptors with deleterious consequences on high acuity and color vision (Bird et al., 1995; Lim et al., 2012).

The etiology of AMD is complex and multifactorial but several lines of evidence associate the disease with local disturbances of lipid metabolism in the ageing human eye (Pauleikhoff et al., 1990). Lipids physiologically accumulate in extracellular deposits known as drusen and sub-retinal drusenoid deposits (SDDs) on the basal and apical side of the RPE, respectively. Drusen contain polar lipids, such as un-esterified (free) cholesterol (UC) and phosphatidylcholine (PC), as well as neutral lipids, such as cholesteryl esters (CEs), and several lipid-binding proteins (apolipoproteins) (Wang et al., 2010; Curcio et al., 2011). The more recently identified SDDs, instead, seem to contain UC only, together with apolipoproteins (Rudolf et al., 2008; Spaide et al., 2018). Drusen (Sarks, 1980) and SDDs (Zweifel et al., 2010) are considered hallmarks of AMD but their actual origin and contribution to the pathology remain unknown. Recently, primary RPE cells isolated from AMD patients, but not from control subjects, were shown to accumulate intracellular lipids *in vitro* (Golestaneh et al., 2017), suggesting altered lipid metabolism in diseased cells.

Genome-wide association studies have linked AMD to several genes involved in generation and remodeling of high-density lipoproteins (HDLs), namely ATP-binding cassette transporter A1 (*ABCA1*), apolipoprotein E (*APOE*), cholesteryl ester transfer protein (*CETP*) and hepatic lipase C (*LIPC*) (Fritsche et al., 2016). A recent review (van Leeuwen et al., 2018) summarizes contradictory results from different studies concerning the association between systemic lipid levels and the risk of developing AMD and links long-term elevated plasma levels of HDL-cholesterol to increased AMD risk. However, it remains unknown whether genes involved in lipid metabolism exert a local and/or a systemic pathogenic effect on the retina.

A gene of interest in this context is *ABCA1*, encoding a transmembrane lipid transporter which generates HDLs together with its partner *ABCG1*. Either transporter uses ATP to flip lipids, mainly UC

and phospholipids (PLs), but also sphingomyelins (SMs) and oxysterols, from the inner leaflet of the plasma membrane to extracellular lipophilic acceptors such as apolipoproteins or nascent HDLs. ABCA1 initiates the formation of HDL by direct interaction with naked apolipoproteins, while ABCG1 requires a lipidated particle (Cavelier et al., 2006; Quazi et al., 2011; Li et al., 2013). Since UC is one of the best established substrates of the two transporters, the ABCA1/ABCG1 pathway is also known as “active cholesterol efflux”. The fundamental role of this pathway for cellular lipid homeostasis is highlighted by macrophage foam cell formation (Tabas, 2002; Favari et al., 2015) and by the progressive and age-dependent lung phenotype, including lipid accumulation in alveolar macrophages and pneumocytes, lung dysfunction and inflammation (Chai et al., 2017) in mice lacking ABCA1, ABCG1 or both. Inhibition of cholesterol efflux leads to cell dysfunction also in pancreatic beta cells (Kruit et al., 2012), neurons (Kruit et al., 2012; Karasinska et al., 2013) and liver cells (Arguello et al., 2015). Liver X receptors (LXR) α and β are the upstream regulators of the pathway: these two transcription factors are activated upon binding of oxysterols that accumulate in conditions of increased UC and upregulate expression of both *ABCA1* and *ABCG1* (Schultz et al., 2000).

Ubiquitous expression of ABCA1 and ABCG1 has been reported in the mouse, monkey and human retina, including the RPE (Tserentsoodol et al., 2006; Duncan et al., 2009; Zheng et al., 2012; Ananth et al., 2014; Zheng et al., 2015; Storti et al., 2017). The function of ABCA1 and ABCG1 in the RPE was previously investigated *in vitro* (Ishida et al., 2006; Duncan et al., 2009; Biswas et al., 2017; Storti et al., 2017; Lyssenko et al., 2018) and shown to mediate transport of UC to ApoA-I, ApoE, HDLs and human serum on both sides of the RPE. This was true for plasma lipoprotein- as well as outer segment (OS)-derived cholesterol. However, the relevance of active cholesterol efflux for the RPE *in vivo* remains unknown. This, together with the fact that the RPE needs an efficient metabolism to handle large amounts of lipids coming from daily OS phagocytosis (Strauss, 2005), prompted us to generate an RPE-specific *Abca1;Abcg1* double knockout (KO) mouse. We characterize the retinal phenotype of this mouse model and provide evidence suggesting a correlation between AMD-associated *ABCA1* genotypes and expression levels of this gene in human cells.

Results

Generation of RPE-specific *Abca1;Abcg1* double KO mice ($RPE^{\Delta Abca1;Abcg1}$)

Expression of ABCA1 and ABCG1 throughout the retinal layers, including the RPE, was confirmed by immunofluorescence (IF) in wild type mouse retinal sections (figure 1A) (Ananth et al., 2014). As previously described for RPE cells *in vitro* (Storti et al., 2017), no co-localization with ezrin (EZR), a marker of the apical microvilli of the RPE, was observed. In order to study the function of ABCA1/ABCG1 in the RPE, we used *BEST1Cre* mice to delete floxed sequences from *Abca1^{flox/flox};Abcg1^{flox/flox}* mice and generate RPE-specific *Abca1;Abcg1* double KOs (called $RPE^{\Delta Abca1;Abcg1}$, see “Materials and methods”, table 1 and figure 1-figure supplement 1). *BEST1Cre* mice express *Cre* recombinase under control of the human bestrophin 1 (*BEST1*, also known as vitelliform macular dystrophy 2, *VMD2*) promoter, resulting in post-natal CRE activity specifically in the RPE (Iacovelli et al., 2011). Although both strains were used before to successfully generate a number of mouse models (Westerterp et al., 2012; Yao et al., 2015; Westerterp et al., 2016; Sundermeier et al., 2017; Ban et al., 2018a; Ban et al., 2018b; Eblimit et al., 2018; Roman et al., 2018), we nonetheless validated the specificity of *Cre* expression in $RPE^{\Delta Abca1;Abcg1}$ mice. High mRNA levels for *Cre* were detected in the eyecup (RPE/choroid) with only a minimal amount of transcripts found in the neural retina, probably due to contamination during eye dissection (figure 1B). To confirm presence of CRE protein in the RPE, we performed IF staining on retinal sections. Although some un-specific staining was observed in the inner retina, CRE-positive nuclei were detected only in the RPE layer of $RPE^{\Delta Abca1;Abcg1}$ but not of control (Ctr, *Cre*-negative) mice (figure 1C). Finally, we checked for successful CRE-mediated excision of floxed fragments by amplifying *Abca1* and *Abcg1* specific sequences from genomic DNA extracted from retina and eyecups (including RPE) of $RPE^{\Delta Abca1;Abcg1}$ and Ctr mice. As expected, deletion of *Abca1* and *Abcg1* was observed in eyecups, but not neural retinas, of *Cre*-positive mice (figure 1D). Even though end-point PCR reactions may not be used to quantify products, the highly variable signal intensities of the amplified *Abca1* and *Abcg1* excised fragments suggested mouse-to-mouse variability in *Cre* expression (figure 1B and data not shown) and/or in deletion efficiency (figure 1D). Of note, the *BEST1Cre* mouse is known to have patchy and variable *Cre* expression in the RPE (Iacovelli et al., 2011; Sundermeier et al., 2017), which could partially explain decreased rather than abolished expression of *Abca1* and *Abcg1* mRNA in eyecups of $RPE^{\Delta Abca1;Abcg1}$ mice (figure 1-figure supplement 2).

Lack of *Abca1* and *Abcg1* in the RPE leads to morphological alterations and intracellular lipid accumulation

Already at 2 months of age, the fundus of RPE^{Δ*Abca1*;Δ*Abcg1*} but not of Ctr mice showed a dotted pattern, possibly reflecting alterations in the pigmentation of RPE cells (figure 2A). Light and electron microscopy on retinal sections revealed an irregular apical RPE border and accumulation of intracellular material resembling lipid droplets (LDs) in RPE^{Δ*Abca1*;Δ*Abcg1*} but not Ctr mice (figure 2B and 2C). Staining with OilRedO (ORO) in retinal sections (figure 2D) and LipidTOX in RPE flat mounts (figure 2E) revealed strong lipid accumulation in CRE-positive RPE cells of RPE^{Δ*Abca1*;Δ*Abcg1*} mice. CRE-negative RPE cells and other retinal layers were ORO-negative and served as internal controls demonstrating the specificity of lipid accumulation in RPE cells lacking *Abca1* and/or *Abcg1*. Both ORO and LipidTOX stain neutral lipids, which constitute the hydrophobic core of LDs (Olofsson et al., 2009). Moreover, actin staining of RPE flat mounts showed morphological irregularities of CRE-positive cells in RPE^{Δ*Abca1*;Δ*Abcg1*} mice when compared to the regular, mainly hexagonal shape of Ctr cells (figure 2F). These morphological irregularities progressively worsened and were more pronounced at 4-6 months of age (figure 3). In particular, double staining for the tight junction protein zona occludens 1 (ZO-1) and the Wnt signaling mediator β-catenin (β-cat) in mutant cells revealed re-localization of β-cat from the plasma membrane to the cytosol, a feature of disorganized RPE (Yang et al., 2018). Pigment epithelial cells in 4-months old RPE^{Δ*Abca1*;Δ*Abcg1*} mice were significantly larger and irregularly shaped (figure 3A, quantification in 3B and 3C). At 6 months, we observed areas of dysmorphic RPE with accumulation of intracellular material and areas of RPE atrophy with infiltration of inflammatory cells (see below) in mutant but not control mice (figure 3D and 3E). Photoreceptor loss correlated with RPE atrophy (see below). Variability of the phenotype within the same retina was probably due to patchy *Cre* expression (figures 1 and 2). Reduced expression levels of *Cre* and the RPE marker monocarboxylic acid transporter 3 (*Mct3*) further indicated atrophic RPE at 6 months of age (figure 3F and 3G). Loss of RPE cells in aged RPE^{Δ*Abca1*;Δ*Abcg1*} mice was most likely a consequence of the lack of ABCA1 and/or ABCG1 activity in RPE rather than of CRE expression *per se*, since *Cre* mRNA levels declined in eyecups of old RPE^{Δ*Abca1*;Δ*Abcg1*} (figure 3F) but not old *BEST1Cre* mice (figure 3-figure supplement 1). Similarly, morphological abnormalities of RPE cells in RPE^{Δ*Abca1*;Δ*Abcg1*} mice were not due to potential CRE toxicity (Thanos et al., 2012; He et al., 2014) as *BEST1Cre* mice only showed minor morphological alterations in the RPE and few bright spots in the fundus, but no lipid accumulation or functional changes (figure 3-figure supplement 2). Thus, lack of *Abca1* and/or *Abcg1*

resulted in lipid accumulation in the RPE and led to several morphological abnormalities that aggravated with time and eventually resulted in RPE cell death.

To exclude developmental effects as a cause for the phenotype, we tested lipid accumulation in the RPE after inactivation of *Abca1* and *Abcg1* in adult mice. For this purpose, we injected an adeno-associated virus (AAV) expressing *Cre* and green fluorescent protein (*GFP*) under the control of the *BEST1* promoter (figure 4A) into the sub-retinal space of adult *Abca1^{flox/flox};Abcg1^{flox/flox}* mice. Although expression levels of *GFP* were variable and difficult to detect in some individual cells, LDs were specifically observed in *GFP*-positive (transduced) cells by LipidTOX staining 10 weeks after AAV injection (figure 4B). In addition, RPE cells in the transduced area appeared larger and less regular than in the non-transduced area, similar to the morphological alterations detected in *RPE^{ΔAbca1;Abcg1}* mice (figure 2F). Lipid accumulation in *Cre-GFP*-positive RPE of *Abca1^{flox/flox};Abcg1^{flox/flox}* mice was further confirmed in retinal sections, which showed ORO-positive lipid staining specifically in the RPE of transduced areas, as well as co-localization of *GFP* and *CRE* signals (figure 4C-F). Contralateral eyes were injected with phosphate buffer saline (PBS, vehicle control) to check for any injection-related effects and showed, as expected, no lipid accumulation (not shown). Taken together, these data indicated altered morphology and intracellular lipid accumulation in adult RPE cells lacking *Abca1* and/or *Abcg1*. This phenotype is in agreement with the known function of ABCA1/ABCG1 as mediators of lipid efflux in the RPE.

Lipid droplets in the RPE of RPE^{ΔAbca1;Abcg1} mice are composed mainly of cholesteryl esters

We next characterized the lipid composition of eyecups from 2-months-old *RPE^{ΔAbca1;Abcg1}* and Ctr mice. We performed the same analysis on the corresponding neural retinas in order to evaluate possible effects of impaired lipid transport in the RPE on lipid homeostasis of other retinal cells. Additionally, plasma samples from the same mice were included to check for presence of any systemic changes on circulating lipid levels that could contribute to the eye phenotype. We used mass spectrometry-based approaches to measure a broad number of lipid classes and species. The analysis revealed significantly increased concentration of CEs in eyecups of *RPE^{ΔAbca1;Abcg1}* mice. In contrast UC, PLs, sphingolipids (SLs) including sphingomyelins (SMs) and ceramides (Cer), and glycerolipids (GLs) including diacylglycerols (DAGs) and triglycerides (TGs) remained unchanged (figure 5A). All of the individual CE species analyzed were more abundant in the mutant mice compared to control littermates. Some CE species were dramatically increased up to 100 fold (figure

5B), including CEs containing fatty acid chains typically found in the retina such as palmitic (16:0), oleic (18:1) and docosahexaenoic (22:6) acid, which is the most abundant fatty acid of photoreceptor OS (Fliesler et al., 1983; Martin et al., 2005; Bretillon et al., 2008). No major difference in the lipid composition was detected in the neural retinas of the two strains (figure 5C), apart from a modest but significant increase in CE levels. However, the small extent of the increase and the low concentration (2.7 ± 1.1 pmol/ μ g protein in the neural retina, 1239.9 ± 955.1 pmol/ μ g protein in the eyecup, table S1) suggested a contamination from the RPE during tissue dissection rather than a real increase in the neural retina. Systemic lipid levels measured in the plasma showed no differences between RPE ^{$\Delta Abca1; Abcg1$} and Ctr mice in any of the considered classes (figure 5D), supporting a local effect of the lack of *Abca1* and *Abcg1* in the RPE. The high variability observed in plasma lipid levels might be explained by the fact that the mice had access to food *ad libitum*, thus, in our experiment, lipid intake was uncontrolled. Analysis of lipid composition therefore revealed prominent accumulation of CEs in the RPE of RPE ^{$\Delta Abca1; Abcg1$} mice without major alterations of the neural retina or plasma lipidomes. Absolute concentrations for all of the analyzed lipid classes can be found in supplementary table S1. Finally, we also detected a significant increase in the relative abundance of the visual cycle intermediates retinyl esters (REs) in eyecups of mutant mice (figure 5E).

Functional consequence of lipid accumulation in the RPE

Since RPE ^{$\Delta Abca1; Abcg1$} mice revealed alterations in RPE morphology and lipid composition, we tested whether lack of *Abca1* and *Abcg1* affected function of the epithelium. For this purpose, we investigated rhodopsin (RHO) regeneration kinetics after bleaching, a major task of the RPE in the classical visual cycle (Strauss, 2005). 2-months-old RPE ^{$\Delta Abca1; Abcg1$} and Ctr mice had similar dark levels of RHO, which were bleached with comparable efficiencies (supplementary table S2). However, RPE ^{$\Delta Abca1; Abcg1$} mice regenerated RHO slower within the first 30 minutes after bleaching. After this initial phase, the amount of regenerated RHO was no longer different between the mice (figure 6 and supplementary table S2). This suggests an early delay in the visual cycle, probably due to difficulties with handling the incoming all-*trans* retinol.

Lack of Abca1 and Abcg1 in the RPE results in age-dependent retinal degeneration

Loss of ABCA1 and ABCG1 from mouse RPE resulted in early lipid accumulation, morphological alterations and atrophy of this cellular layer. To understand the consequences of such diseased RPE

for the neural retina, we imaged the mutant mice at different ages (2, 4 and 6 months) by fundus photography and optical coherence tomography (OCT). The pigmentation changes observed in RPE ^{$\Delta Abca1; Abcg1$} mice at two months of age (figure 2A) worsened at older ages (figure 7A). OCT scans revealed sub-retinal hyper-reflective foci in mutant mice starting at 4 months of age (figure 7A). These foci were accompanied by irregular RPE/outer nuclear layer (ONL) borders and retinal thinning, suggesting ongoing degeneration. Analysis of the respective retinal morphologies (figure 7B) confirmed degenerative processes in the RPE/photoreceptor layers in ageing RPE ^{$\Delta Abca1; Abcg1$} mice. Retinal degeneration was further supported by a significant reduction of the ONL thickness in mutant vs control mice at 6 months of age (figure 7C). The high variability in ONL measurements was likely owed to the patchy expression of the *Cre* transgene resulting in areas with intact RPE/ONL and areas with RPE cell death and consequent photoreceptor degeneration within the same retinal section. In some regions, both RPE and ONL were completely lost (see also figure 3D). The inner retina was instead not affected by ABCA1/ABCG1 knockout in the RPE, as revealed by the determination of the INL thickness and staining for ganglion cells in 6-months-old animals (figure 7-figure supplement 1). Progressing photoreceptor degeneration was also reflected by the retinal function measured by electroretinography (ERG). Scotopic and photopic wave amplitudes gradually decreased in ageing RPE ^{$\Delta Abca1; Abcg1$} mice starting already at 4 months of age (figure 8). In conclusion, lack of *Abca1* and *Abcg1* in the RPE had a strong impact on neural retinal morphology and function, with progressive photoreceptor degeneration.

Inflammatory response in RPE ^{$\Delta Abca1; Abcg1$} mice

Retinal sections analyzed by light microscopy suggested the presence of immune cells in aged mutant mice (figure 3D and 3E) and infiltration of inflammatory cells in the retina is one of the key events in AMD pathogenesis (Kauppinen et al., 2016). We thus stained RPE flat mounts and retinal sections of RPE ^{$\Delta Abca1; Abcg1$} mice for macrophages/activated microglia markers. At 4 months of age, up to about 100 ionized calcium-binding adapter molecule 1 (IBA-1)-positive cells were detected in flat mounts of all mutant RPE at the sites of morphological alterations, but not in non-affected areas (not shown) or Ctr mice. Confocal microscopy showed that IBA-1-positive signals were located within the RPE layer as well as on its basal side (figure 9A, lower cross-sections). Whether they represent cells infiltrating the RPE from the choroidal (basal) side or leaving the retina through the RPE from the apical side was not determined. IBA-1 positive inflammatory cells were also detected in the outer retinal layers

including the sub-retinal space of 6-months old RPE^{ΔAbca1;Abcg1} but not control mice (figure 9B). At this later time point, such cells were not only present in regions of strong photoreceptor and RPE atrophy (not shown, but see figure 3D, E and figure 7B for retinal morphologies showing large, presumably inflammatory cells in the sub-retinal space) but also in retinal regions that were mildly affected (figure 9B). It is conceivable that damaged RPE cells facilitated the movement of IBA-1 positive cells across the RPE layer. Pigmentation of these cells could be due to phagocytosis of melanin granules-rich debris of RPE cells. Increased expression of interleukin 1β (*Il1b*), caspase 1 (*Casp1*) and glial fibrillary acidic protein (*Gfap*) in neural retinas of RPE^{ΔAbca1;Abcg1} mice confirmed a time-dependent inflammatory/stress response upon deletion of *Abca1* and *Abcg1* in the RPE (figure 9C-E).

Single Abca1, but not Abcg1, KO is sufficient to cause early lipid accumulation in the RPE

We initially generated double *Abca1;Abcg1* KO mice in order to completely block the active cholesterol efflux pathway in the RPE. To investigate the individual contribution of each gene to the phenotype, we generated RPE-specific *Abca1* (RPE^{ΔAbca1}) and *Abcg1* (RPE^{ΔAbcg1}) single mutant mice (table 1). Analysis at 2 months of age showed that the RPE morphology of single RPE^{ΔAbca1} mice was similar to the double RPE^{ΔAbca1;Abcg1} mutants (figure 10A). On the other hand, single RPE^{ΔAbcg1} mice were undistinguishable from the Ctr animals (figure 10A). Furthermore, ORO staining confirmed accumulation of neutral lipids in RPE^{ΔAbca1} but not in RPE^{ΔAbcg1} mice (figure 10B), even though CRE was similarly expressed in the RPE layer of all mutant mice (figure 10C). Thus *Abca1* was the main driver of early morphological alterations and lipid accumulation in the RPE.

Decreased ABCA1 expression in human-derived cells carrying the AMD risk-conferring allele of ABCA1

Two SNPs in intron 2 of the human *ABCA1* gene (*rs1883025* and *rs2740488*), which are in high linkage disequilibrium ($r^2=0.941$), have been associated with AMD (Chen et al., 2010; Fauser et al., 2011; Peter et al., 2011; Yu et al., 2011; Fritsche et al., 2016). The major 'C' allele of *rs1883025* and 'A' allele of *rs2740488* have been described to confer increased risk for AMD, while the minor 'T' allele of *rs1883025* and 'C' allele of *rs2740488* were associated with a decreased risk of AMD. However, the effect of these SNPs on *ABCA1* expression and/or function remains unknown. To study the potential effect of the AMD-associated SNPs on *ABCA1* expression, we generated lymphoblastoid cell lines (LCLs) from healthy individuals carrying homozygous decreased (N=3) and increased risk (N=3)

genotypes for the SNPs (table 2). *ABCA1* expression in LCLs was induced by LXR agonist stimulation and mRNA and protein levels were compared between LCLs carrying the different alleles. LCLs derived from subjects homozygous for the AMD increased risk allele of *ABCA1* showed significantly decreased *ABCA1* mRNA expression compared to the reduced risk carriers (figure 11A). A trend towards decreased *ABCA1* expression was observed also at the protein level in carriers of the AMD increased risk genotype (figure 11B and 11C). Even though the difference did not reach significance ($p=0.14$), probably due to the low sample numbers and intrinsic variability, these data provide the first indication of a potential correlation between AMD risk-associated genotypes and decreased *ABCA1* expression, which may impair cholesterol efflux from RPE cells in patients. This finding might be significant for a potential therapy aiming at *ABCA1* gene augmentation (see discussion).

Discussion

Given the link between lipid metabolism and AMD, we generated and characterized a novel RPE-specific *Abca1;Abcg1* KO mouse model (RPE^{Δ*Abca1;Abcg1*}). Although inactivation of the two genes was patchy due to variable *Cre* expression, genetic ablation of *Abca1* and *Abcg1* resulted in strong lipid accumulation in RPE cells (figures 2 and 5). This is in agreement with the known function of ABCA1 and ABCG1 in mediating lipid efflux (Cavelier et al., 2006). Lipid accumulation was accompanied by morphological alterations and, at older ages, loss of RPE cells. Increased size and irregular shape of RPE cells in mutant mice (figure 3) suggested that the healthy cells expanded in order to fill gaps in the epithelium that were generated by the drop out of CRE-positive cells and keep an intact barrier between neural retina and choroid, as previously described (Nagai et al., 1996; Jiang et al., 2014). Nevertheless, discontinuities in the RPE were observed in 6-months-old RPE^{Δ*Abca1;Abcg1*} mice, together with degeneration of photoreceptors in the affected areas (figures 3 and 7). We hypothesize that these were areas where numerous RPE cells were affected by CRE-mediated *Abca1;Abcg1* deletion, resulting in cell death and, therefore, in gaps too large to be filled by expanding neighboring cells. *Abca1* was the main responsible gene for maintaining lipid homeostasis and survival of RPE cells at 2 months of age, since lack of *Abca1*, but not *Abcg1*, was sufficient to cause strong lipid accumulation (figure 10). This is in marked contrast to macrophages where both *Abca1* and *Abcg1* needed to be inactivated to observe a phenotype in non-stressed retinas (Ban et al., 2018a). *Abcg1* may thus be capable to compensate for the loss of *Abca1* in macrophages but may only have a limited ability to do so in the RPE. The reason for this is still unclear but a potential difference in transport substrate specificity between the two cell types can be postulated. Thus, additional experiments are required to conclusively dissect the individual contribution of the two genes to lipid accumulation and impairment of RPE function. Importantly, photoreceptor- and macrophage-specific *Abca1* and/or *Abcg1* KO mice showed a weaker retinal phenotype compared to RPE^{Δ*Abca1;Abcg1*} (Sene et al., 2013; Ban et al., 2018a; Ban et al., 2018b), suggesting that the lipid efflux pathway regulated by *Abca1* and *Abcg1* is of particular importance for the RPE. Furthermore, RPE cells may not be able to easily compensate for the absence of *Abca1* and *Abcg1* by activating alternative mechanisms. RNAseq data for example revealed only very minor alterations in the RPE- and retina-specific transcriptomes of 2-months-old RPE^{Δ*Abca1;Abcg1*} mice (data not shown). This suggests that absence of ABCA1 and ABCG1 in the RPE did not cause strong secondary gene expression changes that could balance the impaired lipid efflux pathway in RPE^{Δ*Abca1;Abcg1*} mice. Taken together, our data demonstrate that proper lipid handling by the

RPE through active cholesterol efflux is essential for maintenance of an intact and functional retina *in vivo*. Moreover, local impairment of the ABCA1-mediated lipid transport activity in the RPE may provide the molecular basis for the genetic link of *ABCA1* to AMD and partially explain the contradictory association between systemic lipid levels and the disease (van Leeuwen et al., 2018).

As mentioned above, prominent intracellular accumulation of LDs was observed in RPE lacking ABCA1/ABCG1 (figure 2). Biochemical analysis of these LDs showed specific accumulation of CEs and, to a lesser extent, REs, while UC as well as PLs, SLs and GLs remained unchanged (figure 5). It is conceivable that the RPE continued to phagocytize lipid-rich OS also in the absence of functional ABCA1/ABCG1 to support photoreceptors. This hypothesis is supported by increased presence of fatty acids typical of OS membranes, such as docosahexaenoic acid (22:6), in the RPE of mutant mice (figure 5A and 5B). The specific accumulation of esterified cholesterol, which is very important for retinal homeostasis (Fliesler et al., 2010; Pikuleva et al., 2014), fits well with the lipid composition of human drusen and SDDs (Haimovici et al., 2001; Wang et al., 2010; Spaide et al., 2018) and with the high cholesterol content in rod OS (Fliesler et al., 1982). The unchanged intracellular levels of UC in eyecups of 2-months-old mutant animals suggest that RPE cells esterified UC and fatty acids from OS disks to generate neutral CEs and REs that can be stored into LDs in an attempt to maintain intracellular UC levels below a toxic threshold (Tabas, 2002; Lakkaraju et al., 2007). Eventually, however, lipid concentration may become too high in the absence of a functional efflux pathway and lead to cell death. In contrast to the RPE, deletion of *Abca1* alone or in combination with *Abcg1* in hepatocytes, the main contributors to systemic lipid levels, not only affected plasma concentrations of UC and CEs, but also those of PLs, TGs and SLs (Timmins et al., 2005; Chung et al., 2010; Iqbal et al., 2018). This difference compared to the RPE suggests once more a cell-type dependent substrate specificity for the lipid efflux pathway or a remodeling of HDLs in the bloodstream, a process that does not occur within cells. Indeed, intracellular lipidomic changes in macrophages and endothelial cells that lacked *Abca1* and *Abcg1* were more similar to the changes identified in RPE cells of RPE ^{$\Delta Abca1; Abcg1$} mice, including an accumulation of cholesterol, both in its un-esterified and esterified forms (Westerterp et al., 2013; Westerterp et al., 2016).

In addition to CEs, the abundance of REs was increased in our model, suggesting that lack of *Abca1* and *Abcg1* not only reduced lipid efflux but also affected intracellular handling of REs as intermediates of the visual cycle (Kiser et al., 2016). An increase in REs and fatty acids may change the kinetics of the enzymes involved in the initial phases of the visual cycle (Saari, 2012). Moreover, altered RPE

apical morphology (figure 2B) could affect the physical interaction between RPE cells and photoreceptor OS, resulting in impaired internalization of incoming all-*trans* retinol intermediates. Once this step is achieved, however, the visual cycle seemed less affected as shown by similar amounts of regenerated RHO at later intervals after bleaching (figure 6). Interestingly, AMD patients show delayed rod-mediated dark adaptation, suggesting visual cycle disturbance, already at early stages of the disease (Owsley et al., 2001; Owsley et al., 2007).

A “cholesterol-recycling” mechanism involving transport of OS-derived cholesterol from the RPE back to the photoreceptors was proposed for the retina (Tserentsoodol et al., 2006). It is rather surprising that retinal function (figure 8), localization of rod and cone markers (not shown), and lipid composition of the neural retina (figure 5C) were not or not strongly affected in young RPE^{ΔAbca1;Abcg1} mice. Thus, photoreceptors seem capable to cope with an impaired lipid supply from RPE. Rods and cones could get enough cholesterol from the healthy CRE-negative RPE cells or they could re-direct towards a different lipid source like the intra-retinal circulation. Since retinal cells are able to synthesize cholesterol (Fliesler et al., 2010), functional cholesterol efflux from the RPE may not be absolutely required for photoreceptor survival. We therefore propose that photoreceptor loss in RPE^{ΔAbca1;Abcg1} mice is a secondary effect to dysfunctional RPE.

In summary, our model recapitulates some important features of dry AMD. i) Impaired lipid efflux in the RPE primarily affects RPE function and survival resulting in secondary photoreceptor degeneration and decreased retinal function in our mice. In both its dry and wet forms, AMD affects RPE cells while many photoreceptors in the macula may be lost secondarily (Rattner et al., 2006; Lim et al., 2012). ii) The phenotype of RPE^{ΔAbca1;Abcg1} mice is age-related and slowly progressing, similar to AMD. iii) The photoreceptor/RPE layer of mutant mice at 4-6 months of age is infiltrated with inflammatory cells, an important hallmark of AMD pathology (Kauppinen et al., 2016).

In addition to the characterization of the mouse model, we present novel preliminary data on the effect of AMD risk-associated SNPs in *ABCA1* on its expression level. No variants in *ABCG1* have so far been associated with the disease, suggesting a predominant role of *ABCA1* in the RPE/retina, an interpretation that fits to the early phenotype of single KO mice in this study (figure 10). Our data from human cells (figure 11) suggest that the AMD increased risk allele correlates with lower *ABCA1* expression, at least upon LXR stimulation. The limited effect of the SNPs on *ABCA1* expression may not be surprising given their intronic location and the relatively small effect size of the SNPs on the disease (odds ratio 0.9 (Fritsche et al., 2016)). Variants in non-coding regions of the genome,

including in the *ABCA1* locus (Rhyne et al., 2009), may directly change gene expression by affecting splicing, chromatin accessibility or binding of transcription factors (Cooper, 2010). On the other hand, we cannot exclude the possibility of an indirect effect due to regions inherited *in cis* with the SNPs or a difference between cell lines in their responsiveness to LXR stimulation. Clearly however, the potential effect of the SNPs on *ABCA1* expression should be confirmed in a larger study, ideally using RPE cells derived from induced pluripotent stem cells (iPSCs) (Leach et al., 2016; Brandl, 2019). Independently of the genotype, it has been reported that expression and function of *ABCA1* is reduced in aged mouse and human monocytes, including in the eye (Sene et al., 2013). Likewise, own preliminary data suggested a tendency of reduced expression of *ABCA1* in eyecups of old human donors (data not shown). It was also shown that cholesterol efflux was less efficient in old compared to young mouse RPE cells (Biswas et al., 2017), further suggesting an age-dependent physiological decline in *ABCA1* expression and function. In the presence of the risk-conferring *ABCA1* allele, expression of the gene may decrease below a critical threshold needed to prevent disease development. If so, this age-dependent decline could be targeted by the pharmacological activation of *ABCA1* gene expression, for example through treatment with an LXR agonist (Koldamova et al., 2014).

Besides the intronic variants being associated with AMD, biallelic mutations in the coding region of *ABCA1* are known to cause the very rare Tangier disease, a systemic condition characterized by virtual absence of plasma HDLs, cholesterol accumulation in several tissues and, in some instances, peripheral neuropathy and increased risk of developing cardiovascular disease (Schaefer et al., 2016). However and in contrast to our mouse data, Tangier patients are not known to have any ophthalmological phenotype, including AMD, except mild corneal opacities (Winder et al., 1996). RPE of Tangier patients might be healthier compared to AMD-affected RPE, making the impact of dysfunctional *ABCA1* weaker in Tangier disease. This might be due to additional impaired mechanisms present in aged/AMD RPE cells, such as oxidative stress, accumulation of bis-retinoids, genetic factors and others.

In conclusion, this study supports an essential role of the *ABCA1*/*ABCG1* lipid efflux pathway for mouse RPE survival *in vivo* and suggests that an impaired lipid metabolism via *ABCA1* may contribute to the pathology of AMD, most likely in combination with additional mechanisms. If the link between *ABCA1* and AMD is confirmed, activation of *ABCA1*-mediated lipid efflux will be an attractive target for AMD therapies.

447 **Materials and methods**448 **Key Resource Table**

| Reagent type (species) or resource | Designation | Source or reference | Identifiers | Additional information |
|---|--|--------------------------|---|--|
| gene (<i>Mus musculus</i>) | <i>Abca1</i> | | NCBI gene ID: 11303 | |
| gene (<i>Mus musculus</i>) | <i>Abcg1</i> | | NCBI gene ID: 11307 | |
| strain, strain background (<i>Mus musculus</i>) | C57BL/6J (wt) | The Jackson Laboratory | RRID:IMSR_JAX:000664; The Jackson Laboratory: 000664 | |
| strain, strain background (<i>Mus musculus</i>) | <i>BEST1Cre</i> | PMID:21212186 | RRID:IMSR_JAX:017557 | Name at the Jackson Laboratory: C57BL/6-Tg(BEST1-cre)1Jdun/J |
| strain, strain background (<i>Mus musculus</i>) | <i>Abca1^{flox/flox}</i> , <i>Abcg1^{flox/flox}</i> | The Jackson Laboratory | RRID:IMSR_JAX:021067 | Name at the Jackson Laboratory: B6.Cg-Abca1tm1Jp Abcg1tm1Tall/J |
| antibody | anti-ABCA1 (rabbit polyclonal) | Novus Biologicals | RRID:AB_10000630; Novus Biologicals: NB400-105 | (1:250 for IF, 1:200 for WB) |
| antibody | anti-ABCG1 (rabbit monoclonal) | Abcam | RRID:AB_867471; Abcam: ab52617 | (1:100) |
| antibody | anti-EZR (mouse monoclonal) | Santa Cruz Biotechnology | RRID:AB_783303; Santa Cruz: sc-58758 | (1:500) |
| antibody | anti-CRE (rabbit polyclonal) | Merck | RRID:AB_10806983; Merck: 69050-3 | (1:300) |
| antibody | anti-IBA1 (rabbit polyclonal) | Wako Fujifilm | RRID:AB_839504; Wako Fujifilm: 019-19741 | (1:500) |
| antibody | anti-ZO1 (rabbit polyclonal) | Thermo Fisher Scientific | RRID:AB_2533456; Thermo Fisher Scientific: 40-2200 | (1:100) |
| antibody | anti-βcatenin (mouse monoclonal) | BD Biosciences | RRID:AB_397554; BD Biosciences: 610153 | (1:300) |
| antibody | anti-POU4F1 (mouse monoclonal) | Merck | RRID:AB_94166; Merck: MAB1585 | (1:100) |
| recombinant DNA reagent | pTR-BEST1-Cre-P2A-GFP (AAV vector plasmid) | This paper | | Constructed from AAV plasmid materials at the University of Florida, laboratory of S. Boye |
| sequence-based reagent | Random Primers | Promega | Promega :C1181 | |
| peptide, recombinant protein | Phalloidin-Alexa488 | Thermo Fisher Scientific | RRID:AB_2315147; Thermo Fisher Scientific: A12379 | (1:100) |
| commercial assay or kit | LipidTOX Red Neutral Lipid Stain | Thermo Fisher Scientific | Thermo Fisher Scientific: H34476 | (1:200) |
| commercial assay or kit | Protease Inhibitors Cocktail | Sigma-Aldrich | Sigma-Aldrich: P2417 | |
| commercial assay or kit | PowerUp Syber Green Master Mix | Thermo Fisher Scientific | Thermo Fisher Scientific: A25742 | |
| commercial assay or kit | NucleoSpin RNA isolation kit | Macherey-Nagel | Macherey-Nagel: 740949.250 | |
| chemical compound, drug | OilRedO (ORO) | Sigma-Aldrich | Sigma-Aldrich: O9755-25G | |
| chemical compound, drug | Oxalic Acid | Sigma-Aldrich | Sigma-Aldrich: 75688 | |

| | | | | |
|-------------------------|--|---|---------------------------------------|---|
| chemical compound, drug | LXR agonist | Roche, PMID:16876993 | Roche: T0901317 | |
| chemical compound, drug | SPLASH® | Avanti Polar Lipids | Avanti Polar Lipids: 330707 | |
| chemical compound, drug | d7-sphinganine (SPH d18:0) | Avanti Polar Lipids | Avanti Polar Lipids: 860658 | D-erythro-sphinganine-d7 |
| chemical compound, drug | d7-sphingosine (SPH d18:1) | Avanti Polar Lipids | Avanti Polar Lipids: 860657 | D-erythro-sphingosine-d7 |
| chemical compound, drug | Dihydroceramide (Cer d18:0/12:0) | Avanti Polar Lipids | Avanti Polar Lipids: 860635 | N-lauroyl-D-erythro-sphinganine |
| chemical compound, drug | Ceramide (Cer d18:1/12:0) | Avanti Polar Lipids | Avanti Polar Lipids: 860512 | N-lauroyl-D-erythro-sphingosine |
| chemical compound, drug | Glucosylceramide (GluCer d18:1/8:0) | Avanti Polar Lipids | Avanti Polar Lipids: 860540 | D-glucosyl-β-1,1'-N-octanoyl-D-erythro-sphingosine |
| chemical compound, drug | Sphingomyelin (SM d18:1/12:0) | Avanti Polar Lipids | Avanti Polar Lipids: 860583 | N-lauroyl-D-erythro-sphingosylphosphorylcholine |
| chemical compound, drug | d7-sphingosine-1-phosphate (S1P d18:1) | Avanti Polar Lipids | Avanti Polar Lipids: 860659 | D-erythro-sphingosine-d7-1-phosphate |
| chemical compound, drug | Methanol | Honeywell | Honeywell: 34860 Riedel-de Haen | |
| chemical compound, drug | MTBE | Sigma-Aldrich | Sigma-Aldrich: 20256 | tert-Butyl methyl ether |
| chemical compound, drug | Chloroform | Sigma-Aldrich | Sigma-Aldrich: 650498 | |
| chemical compound, drug | Acetonitrile | Sigma-Aldrich | Sigma-Aldrich: 534851 | |
| chemical compound, drug | Isopropanol | Sigma-Aldrich | Sigma-Aldrich: 59300 | |
| software, algorithm | ImageJ Tissue Cell Geometry macro | Institute for Research in Biomedicine, Barcelona, Spain | | http://adm.irbbarcelona.org/image-j-fiji |
| software, algorithm | Relative Quantification Software | Thermo Fisher Cloud | | https://www.thermofisher.com/ch/en/home/digital-science/thermo-fisher-connect/all-analysis-modules.html |
| software, algorithm | GraphPad Prism, version 7 | GraphPad | RRID:SCR_002798 | |
| software, algorithm | Tracefinder® Clinical 4.1 | Thermo Fisher Scientific | | |
| other | transcend® TLX I eluting pump | Thermo Fisher Scientific | | |
| other | Q-Exactive® | Thermo Fisher Scientific | | |
| other | Mini-PROTEAN® Precast Gels, 4-15% polyacrylamide | BioRad | BioRad: 4561086DC | |
| other | C30 Accucore® LC column | Thermo Fisher Scientific | Thermo Fisher Scientific: 7826-152130 | 150 mm * 2.1 mm * 2.6 µm |

Mice and genotyping

All animal experiments adhered to the ARVO Statement for the Use of Animals in Ophthalmic and Vision Research and the regulations of the Veterinary Authorities of Kanton Zurich, Switzerland (study approval reference numbers: ZH141/2016 and ZH216/2015). Mice were maintained as breeding colonies at the Laboratory Animal Services Center (LASC) of the University of Zurich in a 14 h: 10 h light-dark cycle with lights on at 6 am and lights off at 8 pm. Mice had access to food and water *ad libitum*. Average light intensity at cage levels was 60–150 lux, depending on the position in the rack. C57BL/6J (Bl6) were used as wild type controls. *BEST1Cre* mice were described earlier (Iacovelli et al., 2011). *Abca1;Abcg1* double floxed mice (*Abca1^{flox/flox};Abcg1^{flox/flox}*) were purchased from The Jackson Laboratory (Bar Harbor, ME, USA). Founder mice were on a Bl6 background and were genotyped for absence of known spontaneous mutations leading to retinal degeneration (*rd1*, *rd8*, *rd10*, *Cpfl1* and *Gpr179*). Mice were crossed in order to generate double- and single-floxed *Cre*-positive mice and *Cre*-negative littermate controls. All breeding pairs were heterozygous for *BEST1Cre*. Primers listed in supplementary table 3 (table S3) were used to genotype the mice by conventional PCR using genomic DNA extracted from ear biopsies or eye tissues. Although ocular expression of the *BEST1Cre* transgene is restricted to post-natal RPE (Iacovelli et al., 2011) and figure 1C), *BEST1Cre* can be expressed in other cell types, such as melanocytes (Sundermeier et al., 2017) and Sertoli cells of the testis (Masuda et al., 2010; Milenkovic et al., 2015). Probably due to ectopic expression of the transgene in germ-line cells, we occasionally observed systemic or mosaic heterozygous KO animals for *Abca1* and/or *Abcg1* (figure 1-figure supplement 1A). We controlled for presence of the excised allele in ear biopsies to avoid generation of full KO animals and defined our mice as shown in table 1.

Since a heterozygous *flox/-* genotype resulted in a 50% reduction of the *Abca1* and *Abcg1* transcripts in non *Cre*-expressing tissues (figure 1-figure supplement 1B), we excluded the possibility that systemic lack of one functional *Abca1* and/or *Abcg1* allele had an impact on the observed phenotype. To this aim, eyes of *Cre*-negative heterozygous animals (*Abca1^{flox/-};Abcg1^{flox/flox}*, *Abca1^{flox/flox};Abcg1^{flox/-}*, or *Abca1^{flox/-};Abcg1^{flox/-}*) were analyzed up to 6 months of age. No difference to *Abca1^{flox/flox};Abcg1^{flox/flox}* controls were found (retinal morphology in figure 1-figure supplement 1C and ERG data not shown). All *BEST1Cre*-negative mice were therefore used as control animals.

AAV generation and injection

A Cre-expression cassette was fused to GFP via a porcine teschovirus 2A (P2A) sequence and cloned downstream of the RPE-specific human *BEST1* promoter into the *pTR* vector. *pTR-BEST1-Cre-P2A-GFP* was packaged into AAV4 capsid at the Viral Vector Facility of the Neuroscience Center Zurich (ZNZ), University of Zurich, Switzerland. 7.3×10^9 viral genomes/eye (1 μ L volume) were injected into the sub-retinal space of *Abca1^{flox/flox};Abcg1^{flox/flox}* mice as previously described (Barben et al., 2018a). Mice were injected at 4-15 weeks of age and sacrificed 10 weeks post-injection. Eyes were marked nasally by cauterization and fixed for subsequent IF/lipid staining as described below.

Morphology, light microscopy and transmission electron microscopy

Eyes were marked dorsally by cauterization and prepared as described (Barben et al., 2018a). 500 nm nasal-temporal sections were analyzed by light microscopy (Zeiss Axioplan, Feldbach, Switzerland) and Adobe Photoshop CS6 (Adobe Systems Inc., San Jose, CA, USA) was used to photomerge high magnification images of the outer and inner retina as well as to create retina panoramas. Images at higher magnification were always acquired from the central region close to the optic nerve head. The ruler tool of Adobe Photoshop CS6 was used to measure ONL and INL thickness at the indicated distance from optic nerve head in retinal panoramas. For transmission electron microscopy, ultrathin sections (50 nm) were cut, stained with uranyl acetate and lead citrate and analyzed using a Philips CM100 transmission electron microscope (Philips, Amsterdam, The Netherlands).

IF on retinal sections, ORO staining and RPE flat mounts

Eyes were marked dorsally by cauterization and retinal 12 μ m nasal-temporal cryosections were prepared as described (Barben et al., 2018b). For AAV-injected animals, eyes were marked nasally and dorsal-ventral sections were cut. Sections were blocked in blocking solution (3% normal goat serum, 0.3% Triton X-100 in 0.1 M PB) for 1 h at room temperature (RT), followed by overnight incubation at 4°C with the following primary antibodies: rabbit anti-ABCA1 (1:250, NB400-105, Novus Biologicals, Littleton, CO, USA), rabbit anti-ABCG1 (1:100, ab52617, Abcam, Cambridge, UK), mouse anti-EZR (1:500, sc-58758, Santa Cruz Biotechnology, Dallas, TX, USA), rabbit anti-CRE (1:300, 69050-3, Merck, Darmstadt, Germany), rabbit anti-IBA-1 (1:500, 019-19741, Wako Fujifilm, Neuss, Germany) or mouse anti-POU4F1 (1:100, MAB1585, Merck). After 3 washing steps in PB salt (0.1 M PB with the addition of 0.8% NaCl and 0.02% KCl), samples were incubated at RT for 2 h with

appropriate secondary antibodies conjugated to Cy2, Cy3 or AlexaFluor555 fluorophores (Jackson ImmunoResearch, Suffolk, UK and Thermo Fisher Scientific, Reinach, Switzerland). Nuclei were counterstained with 4',6-Diamidine-2'-phenylindole di-hydrochloride (DAPI, Thermo Fisher Scientific), sections were mounted with Mowiol and imaged using a fluorescent microscope (Zeiss Axioplan). Sections stained with secondary antibody only were used as negative controls.

For neutral lipid ORO staining, cryosections were washed with distilled H₂O and incubated in 0.2% KMnO₄ for 40 min at RT, followed by neutralization with fresh 1% oxalic acid for 1-2 min to bleach the melanin pigment in the RPE/choroid. After 2 washing steps in H₂O, sections were rinsed with 60% isopropanol and incubated for 10 min at RT in 0.42% ORO working solution (Sigma-Aldrich, Merck, Buchs SG, Switzerland; 0.7% ORO stock solution in isopropanol diluted 3:2 in H₂O to generate the working solution). Sections were rinsed with 60% isopropanol, washed twice with H₂O and nuclei were counterstained with enhanced Meyer's hematoxylin (Artechemis, Zofingen, Switzerland) for 1-2 min. Sections were mounted with Mowiol and imaged using light microscopy within 15 days (Leica Microsystems, Heerbrugg, Switzerland).

RPE flat mounts were prepared as described (Oczos et al., 2014). After washing, samples were incubated for 1 h at RT in blocking solution (see above), followed by overnight incubation at 4°C with primary antibodies: rabbit anti-CRE (see above), rabbit anti-ZO-1 (1:100, 40-2200, Thermo Fisher Scientific), mouse anti-β-cat (1:300, 610153, BD Biosciences, Allschwil, Switzerland) or rabbit anti-IBA-1 (see above). After 3 washing steps in PB salt, samples were incubated at RT for 2 h with appropriate secondary antibodies as described above or phalloidin-AlexaFluor488 to stain F-actin (1:100, A12379, Thermo Fisher Scientific). Nuclei were counterstained with Hoechst (2 µg/ml, Sigma-Aldrich) and lipids with LipidTOX (1:200, H34476, Thermo Fisher Scientific) for 30 min at RT. Samples were mounted on glass slides with Mowiol and imaged using a fluorescent microscope (Zeiss Axioplan) or an SP8 inverted confocal microscope (Leica Microsystems). Three ZO-1-stained images per RPE flat mount quadrant (dorsal, ventral, nasal and temporal of the optic nerve head) were used for quantification with the Tissue Cell Geometry macro in ImageJ (developed by the Institute for Research in Biomedicine, Barcelona, Spain, <http://adm.irbbarcelona.org/image-j-fiji>). At least N=998 RPE cells per group (N=3-4 mice) were examined. The ratio between the major and minor axis of the fitted ellipse was used as a readout of cell shape.

Plasma and eye tissue collection for lipid analysis

After a lethal dose of anesthesia, blood was collected by cardiac puncture using a 1 ml syringe and 26G needle into Microtainer K₂-EDTA-coated tubes (BD Biosciences). Tubes were inverted 20 times, plasma was separated by centrifugation at 2'500 g for 10 min at RT and snap-frozen in liquid nitrogen (N₂). Neural retinas were isolated through a slit in the cornea and snap-frozen in liquid N₂; corresponding eyecups (containing RPE) were isolated and dissected from contaminating cornea, optic nerve or adipose tissue left overs. For analysis of UC, CEs and REs, tissues from both eyes of the same animal were pooled; whereas for analysis of PLs, SLs and GLs, tissues from single eyes were analyzed. For analysis of UC, CEs and REs, eyecup samples were enriched for RPE cells by incubating the tissues in 100 µl of PBS for 20 min at RT followed by flicking of the tubes 50 times to release pigmented cells into the PBS, similar to a procedure previously used for protein isolation (Wei et al., 2016). Remaining posterior eyecups were removed and samples snap-frozen in liquid N₂. These samples were labelled as 'RPE-enriched eyecup' (figure. 5). For analysis of PLs, SLs and GLs, complete eyecups were snap-frozen in liquid N₂. These samples were labelled as 'whole eyecup' (figure. 5). After thawing, 100 µl of PBS were added to each tissue. All samples were then homogenized by sonication, 20 µl of 0.6% Triton in PBS were added to each tube (final concentration: 0.1% Triton) and samples were incubated on a rotating wheel for 1 h at 4°C. Samples were centrifuged at 1'000 g for 3 min at RT and supernatant used for protein quantification using the bicinchoninic acid assay (BCA, Thermo Fisher Scientific) followed by lipid extraction.

Lipid extraction

Lipid extraction was performed as described previously (Pellegrino et al., 2014) with some modifications. For UC, CEs and REs, 1 ml of a methanol:MTBE:chloroform (MMC) mixture 4:3:3 (v/v/v) was added to 20 µl plasma or 50 µg protein of tissue homogenate. The MMC mix was fortified with 100 pmoles of d7-cholesterol and d7-CE 16:0 (Avanti Lipids, Alabaster, AL, USA). Samples were briefly vortexed and mixed on a shaker at 37°C (1'400 rpm, 20 min). Protein precipitation was obtained after centrifugation for 5 min, 16'000 g, 25°C. The single-phase supernatant was collected, dried under N₂ and stored at -20°C until analysis. Dried lipids were dissolved in 100 µl methanol. For PLs, SLs and GLs, 1 ml of MMC mixture 1.33:1:1 was added to 20 µl of plasma or tissue homogenate. The MMC was fortified with the SPLASH mix of internal standards and 100 pmoles/ml of the following internal standards (all from Avanti Lipids): d7-sphinganine (SPH d18:0), d7-sphingosine (SPH d18:1),

dihydroceramide (Cer d18:0/12:0), ceramide (Cer d18:1/12:0), glucosylceramide (GluCer d18:1/8:0), sphingomyelin (SM d18:1/12:0) and 50 pmoles/ml d7-sphingosine-1-phosphate (S1P d18:1). Samples were briefly vortexed and mixed on a shaker at 25°C (950 rpm, 30 min). Protein precipitation was obtained after centrifugation for 10 min, 16'000 g, 25°C. The single-phase supernatant was collected, dried under N₂ and stored at -20°C until analysis. Dried lipids were dissolved in 100 µL methanol:isopropanol (1:1, v/v).

Lipid analysis

Liquid chromatography was done according to (Narváez-Rivas et al., 2016) with some modifications. Lipids were separated using a C30 Accucore LC column (150 mm * 2.1 mm * 2.6 µm) and a transcend TLX eluting pump (Thermo Fisher Scientific). UC, CEs and REs were separated with the following mobile phases: A) acetonitrile:water (2:8 v/v) with 10 mM ammonium acetate and 0.1 % formic acid, B) isopropanol:acetonitrile (9:1 v/v) with 10 mM ammonium acetate and 0.1 % formic acid and C) methanol at a flow rate of 0.3 ml/min. The following gradient was applied: 0.0-1.5 min (isocratic 70% A, 20% B and 10% C), 1.5-18.5 min (ramp 20-100% B), 18.5-25.5 min (isocratic 100% B) and 25.5-30.5 minutes (isocratic 70% A, 20% B and 10% C). PLs, SLs and GLs were separated with the following mobile phases: A) acetonitrile:water (6:4 v/v) with 10 mM ammonium acetate and 0.1% formic acid and B) as above at a flow rate of 0.26 ml/min. The following gradient was applied: 0.0-0.5 minutes (isocratic 30% B), 0.5-2 minutes (ramp 30-43% B), 10-12.0 minutes (ramp 43-55% B), 12.0-18.0 minutes (ramp 65-85% B), 18.0-20.0 minutes (ramp 85%-100% B), 20-35 minutes (isocratic 100% B), 35-35.5 minutes (ramp 100-30% B) and 35.5-40 minutes (isocratic 30% B).

The liquid chromatography was coupled to a hybrid quadrupole-orbitrap mass spectrometer Q-Exactive (Thermo Fisher Scientific). For UC, CEs and REs, samples were analyzed in positive mode using a heated electrospray ionization (HESI) interface. The following parameters were used: spray voltage 3.5 kV, vaporizer temperature of 300 °C, sheath gas pressure 20 AU, aux gas 8 AU and capillary temperature of 320 °C. The detector was set to an MS2 method using a data-dependent acquisition with top10 approach with stepped collision energy between 25 and 30. A 140'000 resolution was used for the full spectrum and a 17'500 for MS2. A dynamic exclusion filter was applied which excluded fragmentation of the same ions for 20 sec. For PLs, SLs and GLs, a data-dependent acquisition with positive and negative polarity switching was used. A full scan was used from 220-3'000 m/z at a resolution of 70'000 and AGC Target 3e6 while data-dependent scans (top10) were

acquired using normalized collision energies (NCE) of 25, 30 and a resolution of 17'500 and AGC target of 1e5.

Identification criteria for UC, CEs and REs were 1) resolution with an accuracy of 5 ppm from the predicted mass at a resolving power of 140'000 at 200 m/z, 2) matching retention time on synthetic available standards and 3) the specific fragmentation patterns ($[M-H_2O]^+$ and 369.3 for cholesterol esters and 269.2 for retinyl esters). Identification criteria for PLs, SLs and GLs were 1) resolution with an accuracy of 5 ppm from the predicted mass at a resolving power of 70'000 at 200 m/z, 2) isotopic pattern fitting to expected isotopic distribution, 3) comparison of the expected retention time to an in-house database and 4) fragmentation pattern matching to an in-house experimentally validated lipid fragmentation database. Quantification was done using single point calibration or by comparing the area under the peak of each species to the area under the peak of the internal standard. Quality controls using a mixture of all samples were used in 4 concentration (1x, 0.5x, 0.25x and 0.125x). Triplicates on the quality controls were measured, and the CV% for each of the lipids reported was below 20%. Mass spectrometric data analysis was performed in Treacefinder software 4.1 (Thermo Fisher Scientific) for peak picking, annotation and matching to the in-house fragmentation database.

Fundus imaging/OCT and ERG

Pupils were dilated using Cyclogyl 1% (Alcon Pharmaceuticals, Fribourg, Switzerland) and Neosynephrine 5% (Ursapharm Schweiz GmbH, Roggwil, Switzerland) 20 min prior to anesthesia. Mice were anesthetized by subcutaneous injection of ketamine (85 mg/kg, Parke-Davis, Berlin, Germany) and Xylazine (4 mg/kg, Bayer AG, Leverkusen, Germany) and a drop of 2% Methocel (OmniVision AG, Neuhausen, Switzerland) was applied to keep the eyes moist. Mice were placed on a heated pad and fundus images and OCT scans were acquired using the Micron IV system (Phoenix Research Labs, Pleasanton, CA, USA).

ERG recordings were performed as described (Kast et al., 2016). Briefly, mice were dark-adapted overnight, pupils dilated and animals anesthetized as described above. A drop of Mydriaticum Dispersa (OmniVision AG) was applied to induce mydriasis and to keep the tissue moist. A reference electrode was inserted subcutaneously between the eyes, a ground electrode was inserted subcutaneously at tail base and recording gold electrodes were placed onto mouse corneas. Mice were placed on a heated pad in front of a Ganzfeld chamber. Responses to 14 different light intensities ranging from -50 db ($0.000025 \text{ cd} \cdot \text{s/m}^2$) to 15 db ($79 \text{ cd} \cdot \text{s/m}^2$) for scotopic and 8 different

light intensities ranging from -10 db (25 cd*s/m²) to 25 db (790 cd*s/m²) for photopic conditions were recorded using an LKC UTAS Bigshot recording unit (LKC Technologies Inc., Gaithersburg, MD, USA). Mice were light-adapted for 5 min before photopic recordings. Ten recordings were averaged per light intensity; responses from the left and right eye of the same animal were averaged for subsequent analysis.

Measurement of rhodopsin regeneration kinetics

All mice used for this experiment were homozygous for the *Rpe65*_{450Met} variant. RHO regeneration was measured as previously described (Wenzel et al., 2005; Samardzija et al., 2008). Briefly, mice were dark-adapted overnight. After pupil dilation, mice were exposed to 5'000 lux of white light for 10 min, a light intensity and exposure duration that does not induce retinal damage in these mice. Mice were returned to darkness for the indicated time points (30, 60 or 120 min) or euthanized immediately. After euthanasia, retinas were isolated in darkness through a slit in the cornea and snap-frozen in N₂. RHO content was measured as described (Wenzel et al., 2005).

Human subject recruitment, LCL generation and culture

The study was approved by the local ethical committees at the Radboud University Medical Center and was performed in accordance with the tenets of the Declaration of Helsinki. Individuals were selected from the European Genetic Database (EUGENDA, <https://www.eugenda.org/>), a large multicenter database for clinical and molecular analysis of AMD, and provided written informed consent before participation. Disease status was determined based on classification of color fundus photographs and, if available, spectral domain OCT and fluorescein angiography by certified graders as previously described (Ristau et al., 2014). LCLs were generated for six control subjects, defined as individuals having only pigmentary changes, less than 10 small drusen or without macular abnormalities. Human B-lymphocytes were immortalized by transformation with the Epstein-Barr virus according to established procedures (Wall et al., 1995). LCLs were generated for three control individuals who were homozygous for *ABCA1* genotypes conferring decreased risk for AMD (*rs1883025* TT and *rs2740488* CC) and for three control individuals who were homozygous for *ABCA1* genotypes conferring increased risk for AMD (*rs1883025* CC and *rs2740488* AA), as shown in table 2. DNA samples were genotyped with a custom-modified Illumina HumanCoreExome array (Illumina, Eindhoven, Netherlands) at the Center for Inherited Disease Research (CIDR, Baltimore, MD, USA).

and quality control and genotype imputation using the 1000 Genomes Project reference panel (McVean et al., 2012) were performed by the International AMD Genomic Consortium as previously described (Fritsche et al., 2016). *ABCA1* rs1883025 genotypes were additionally confirmed by sequencing of a PCR fragment flanking the SNP on genomic DNA extracted from 1×10^6 cells. Sequencing results matched the human *ABCA1* locus, proving the human origin of the cell lines (data not shown). LCLs were also checked for absence of mycoplasma contamination via PCR using primers specific for the mycoplasma genome in the medium of confluent cultures (data not shown). LCLs were cultured in a humid incubator at 37°C and 5% CO₂ in RPMI 1640 medium (Sigma-Aldrich) supplemented with 15% heat-inactivated fetal bovine serum (Gibco, Thermo Fisher Scientific), 20 mM HEPES buffer (Sigma-Aldrich) and 10'000 U/mL penicillin-streptomycin (Gibco). Cells were seeded at a concentration of $0.5-1 \times 10^6$ cells/ml and split every 3-4 days. For experiments, $2-3 \times 10^6$ cells per condition were seeded in 6-well plates and stimulated with 1 μ M LXR agonist (T0901317; prepared at Roche as previously reported (Panday et al., 2006)) or DMSO vehicle control for 24 h. LCLs were then washed with PBS and harvested for RNA or protein analysis (see below).

Gene expression analysis

RNA was extracted from neural retina and eyecups (containing RPE and choroid) using an RNA isolation kit (Macherey-Nagel, Oensingen, Switzerland) with on column DNaseI treatment and used for cDNA synthesis with oligo-dT as previously described (Samardzija et al., 2006; Storti et al., 2017). For human LCL samples, RNA was isolated as above but 0.5 μ g random primers (Promega, Dübendorf, Switzerland) were used instead of oligo-dT for cDNA synthesis. Transcript levels in 10 ng of cDNA were measured by semi-quantitative real-time PCR using an ABI QuantStudio3 machine (Thermo Fisher Scientific) with the PowerUp Sybr Green master mix (Thermo Fisher Scientific) and primer pairs specific for the genes of interest (supplementary table S4). Primers were designed to span large introns and avoid known SNPs. Beta-actin (*Actb*) was used to normalize mouse gene expression with the comparative threshold cycle method ($\Delta\Delta C_t$) of the Relative Quantification software of the Thermo Fisher Cloud. For LCL samples, *ACTB* and *RPL28* levels were used for double normalization with the same method. Note that in order to measure possible decrease in *Abca1* and *Abcg1* transcripts in KO mice, primers were designed to amplify part of the excised region (exons 45 and 46 for *Abca1* and exon 3 for *Abcg1*).

Protein isolation from LCLs and Western Blotting (WB)

Cells were collected, washed twice with ice-cold PBS and lysed in 50 µl of RIPA buffer supplemented with protease inhibitor cocktail (P2417, Sigma-Aldrich) for 15 min on ice. After centrifugation at 16'000 g for 15 min at 4°C, supernatant was collected and protein concentration measured by BCA. 50 µg of proteins were loaded on 4-15% polyacrylamide gradient gels (Bio-Rad, Cressier, Switzerland) for SDS-PAGE followed by semi-dry transfer to a nitrocellulose membrane. Membranes were blocked in 5% non-fat blocking milk (Bio-Rad) for 1 h at room temperature prior to incubation overnight at 4°C with primary antibodies: rabbit anti-ABCA1 (1:200, NB400-105, Novus Biologicals) and mouse anti-ACTB (1:10'000, A5441, Sigma-Aldrich). After washing, membranes were incubated with appropriate horseradish peroxidase (HRP)-conjugated secondary antibodies for 1-2 h at RT. Signals were developed using enhanced chemiluminescence (ECL) substrate (PerkinElmer, Schwerzenbach, Switzerland) and visualized using X-ray films. Intensity of bands was quantified using ImageJ and normalized to ACTB levels.

Statistical analysis

The number of biological replicates is defined in figure legends as “N” and refers to the number of individual animals or cell lines analyzed in this study. The number of technical replicates may be indicated in the corresponding figure legend as well, when appropriate. All statistical analysis, as indicated in figure legends, were performed using GraphPad Prism 7 (San Diego, CA, USA).

Acknowledgments

The authors would like to thank Cornelia Imsand, Sarah Nötzli, Adrian Urwyler, Andrea Gubler and Ana Bordonhos (University of Zurich) for excellent technical support and Dr. Everson Nogoceke (Roche pRED) for helpful discussions.

References

- Ananth, S., Gnana-Prakasam, J. P., Bhutia, Y. D., Veeranan-Karmegam, R., Martin, P. M., Smith, S. B., & Ganapathy, V. (2014). Regulation of the cholesterol efflux transporters ABCA1 and ABCG1 in retina in hemochromatosis and by the endogenous siderophore 2,5-dihydroxybenzoic acid. *Biochimica et Biophysica Acta (BBA) - Molecular Basis of Disease*, 1842(4), 603-612. doi:10.1016/j.bbadis.2014.01.010
- Arguello, G., Balboa, E., Arrese, M., & Zanlungo, S. (2015). Recent insights on the role of cholesterol in non-alcoholic fatty liver disease. *Biochimica et Biophysica Acta (BBA) - Molecular Basis of Disease*, 1852(9), 1765-1778. doi: 10.1016/j.bbadis.2015.05.015
- Ban, N., Lee, T. J., Sene, A., Choudhary, M., Lekwuwa, M., Dong, Z., . . . Apte, R. S. (2018a). Impaired monocyte cholesterol clearance initiates age-related retinal degeneration and vision loss. *JCI Insight*, 3(17). doi:10.1172/jci.insight.120824
- Ban, N., Lee, T. J., Sene, A., Dong, Z., Santeford, A., Lin, J. B., . . . Apte, R. S. (2018b). Disrupted cholesterol metabolism promotes age-related photoreceptor neurodegeneration. *Journal of Lipid Research*, 59(8), 1414-1423. doi:10.1194/jlr.M084442
- Barben, M., Ail, D., Storti, F., Klee, K., Schori, C., Samardzija, M., . . . Grimm, C. (2018a). Hif1a inactivation rescues photoreceptor degeneration induced by a chronic hypoxia-like stress. *Cell Death and Differentiation*. doi:10.1038/s41418-018-0094-7
- Barben, M., Schori, C., Samardzija, M., & Grimm, C. (2018b). Targeting Hif1a rescues cone degeneration and prevents subretinal neovascularization in a model of chronic hypoxia. *Molecular Neurodegeneration*, 13(1), 12. doi:10.1186/s13024-018-0243-y
- Bird, A. C., Bressler, N. M., Bressler, S. B., Chisholm, I. H., Coscas, G., Davis, M. D., . . . Klein, R. (1995). An international classification and grading system for age-related maculopathy and age-related macular degeneration. The International ARM Epidemiological Study Group. *Survey of Ophthalmology*, 39(5), 367-374. doi:https://doi.org/10.1016/S0039-6257(05)80092-X
- Biswas, L., Zhou, X., Dhillon, B., Graham, A., & Shu, X. (2017). Retinal pigment epithelium cholesterol efflux mediated by the 18 kDa translocator protein, TSPO, a potential target for treating age-related macular degeneration. *Human Molecular Genetics*, 26(22), 4327-4339. doi:10.1093/hmg/ddx319
- Brandl, C. (2019). Generation of Functional Retinal Pigment Epithelium from Human Induced Pluripotent Stem Cells. In B. H. F. Weber & T. Langmann (Eds.), *Retinal Degeneration: Methods and Protocols* (pp. 87-94). New York, NY: Springer New York. doi:10.1007/978-1-4939-8669-9_6
- Bretillon, L., Thuret, G., Grégoire, S., Acar, N., Joffre, C., Bron, A. M., . . . Creuzot-Garcher, C. P. (2008). Lipid and fatty acid profile of the retina, retinal pigment epithelium/choroid, and the lacrimal gland, and associations with adipose tissue fatty acids in human subjects. *Experimental Eye Research*, 87(6), 521-528. doi:10.1016/j.exer.2008.08.010
- Cavelier, C., Lorenzi, I., Rohrer, L., & von Eckardstein, A. (2006). Lipid efflux by the ATP-binding cassette transporters ABCA1 and ABCG1. *Biochimica et Biophysica Acta (BBA) - Molecular and Cell Biology of Lipids*, 1761(7), 655-666. doi:10.1016/j.bbalip.2006.04.012
- Chai, A. B., Ammit, A. J., & Gelissen, I. C. (2017). Examining the role of ABC lipid transporters in pulmonary lipid homeostasis and inflammation. *Respiratory Research*, 18(1), 41. doi:10.1186/s12931-017-0526-9
- Chen, W., Stambolian, D., Edwards, A. O., Branham, K. E., Othman, M., Jakobsdottir, J., . . . Swaroop, A. (2010). Genetic variants near TIMP3 and high-density lipoprotein-associated loci influence susceptibility to age-related macular degeneration. *Proceedings of the National Academy of Sciences*, 107(16), 7401-7406. doi:10.1073/pnas.0912702107
- Chung, S., Timmins, J. M., Duong, M., Degirolamo, C., Rong, S., Sawyer, J. K., . . . Parks, J. S. (2010). Targeted deletion of hepatocyte ABCA1 leads to very low density lipoprotein triglyceride overproduction and low density lipoprotein hypercatabolism. *The Journal of Biological Chemistry*, 285(16), 12197-12209. doi:10.1074/jbc.M109.096933
- Cooper, D. N. (2010). Functional intronic polymorphisms: Buried treasure awaiting discovery within our genes. *Human genomics*, 4(5), 284-288. doi:10.1186/1479-7364-4-5-284
- Curcio, C. A., Johnson, M., Rudolf, M., & Huang, J.-D. (2011). The oil spill in ageing Bruch membrane. *British Journal of Ophthalmology*, 95(12), 1638-1645. doi:10.1136/bjophthalmol-2011-300344
- Duncan, K. G., Hosseini, K., Bailey, K. R., Yang, H., Lowe, R. J., Matthes, M. T., . . . Duncan, J. L. (2009). Expression of reverse cholesterol transport proteins ATP-binding cassette A1 (ABCA1) and scavenger receptor BI (SR-BI) in the retina and retinal pigment epithelium. *British Journal of Ophthalmology*, 93(8), 1116-1120. doi:10.1136/bjo.2008.144006

- Eblimit, A., Agrawal, S. A., Thomas, K., Anastassov, I. A., Abulikemu, T., Mardon, G., & Chen, R. (2018). Conditional loss of *Spat7* in photoreceptors causes progressive retinal degeneration in mice. *Experimental Eye Research*, 166, 120-130. doi:10.1016/j.exer.2017.10.015
- Fausser, S., Smailhodzic, D., Caramoy, A., van de Ven, J. P. H., Kirchhof, B., Hoyng, C. B., . . . den Hollander, A. I. (2011). Evaluation of serum lipid concentrations and genetic variants at high-density lipoprotein metabolism loci and TIMP3 in age-related macular degeneration. *Investigative Ophthalmology and Visual Science*, 52(8), 5525-5528. doi:10.1167/iov.10-6827
- Favari, E., Chroni, A., Tietge, U. J. F., Zanotti, I., Escolà-Gil, J. C., & Bernini, F. (2015). Cholesterol Efflux and Reverse Cholesterol Transport. In A. von Eckardstein & D. Kardassis (Eds.), *High Density Lipoproteins: From Biological Understanding to Clinical Exploitation* (pp. 181-206). Cham: Springer International Publishing. doi:10.1007/978-3-319-09665-0_4
- Fliesler, S. J., & Anderson, R. E. (1983). Chemistry and metabolism of lipids in the vertebrate retina. *Progress in Lipid Research*, 22(2), 79-131.
- Fliesler, S. J., & Bretillon, L. (2010). The ins and outs of cholesterol in the vertebrate retina. *Journal of Lipid Research*, 51(12), 3399-3413. doi:10.1194/jlr.R010538
- Fliesler, S. J., & Schroepfer, G. J. J. (1982). Sterol composition of bovine retinal rod outer segment membranes and whole retinas. *Biochimica et Biophysica Acta (BBA)*, 711(1), 138-148.
- Fritsche, L. G., Igl, W., Bailey, J. N. C., Grassmann, F., Sengupta, S., Bragg-Gresham, J. L., . . . Heid, I. M. (2016). A large genome-wide association study of age-related macular degeneration highlights contributions of rare and common variants. *Nat Genet*, 48(2), 134-143. doi:10.1038/ng.3448
- Golestaneh, N., Chu, Y., Xiao, Y.-Y., Stoleru, G. L., & Theos, A. C. (2017). Dysfunctional autophagy in RPE, a contributing factor in age-related macular degeneration. *Cell Death Dis*, 8, e2537. doi:10.1038/cddis.2016.453
- Haimovici, R., Gantz, D. L., Rumelt, S., Freddo, T. F., & Small, D. M. (2001). The Lipid Composition of Drusen, Bruch's Membrane, and Sclera by Hot Stage Polarizing Light Microscopy. *Investigative Ophthalmology and Visual Science*, 42(7), 1592-1599.
- He, L., Marioutina, M., Dunaief, J. L., & Marneros, A. G. (2014). Age- and Gene-Dosage-Dependent Cre-Induced Abnormalities in the Retinal Pigment Epithelium. *The American Journal of Pathology*, 184(6), 1660-1667. doi:10.1016/j.ajpath.2014.02.007
- Iacovelli, J., Zhao, C., Wolkow, N., Veldman, P., Gollomp, K., Ojha, P., . . . Dunaief, J. L. (2011). Generation of Cre transgenic mice with postnatal RPE-specific ocular expression. *Investigative Ophthalmology and Visual Science*, 52(3), 1378-1383. doi:10.1167/iov.10-6347
- Iqbal, J., Walsh, M. T., Hammad, S. M., Cuchel, M., Rader, D. J., & Hussain, M. M. (2018). ATP binding cassette family A protein 1 determines hexosylceramide and sphingomyelin levels in human and mouse plasma. *Journal of Lipid Research*, 59(11), 2084-2097. doi:10.1194/jlr.M087502
- Ishida, B. Y., Duncan, K. G., Bailey, K. R., Kane, J. P., & Schwartz, D. M. (2006). High density lipoprotein mediated lipid efflux from retinal pigment epithelial cells in culture. *British Journal of Ophthalmology*, 90(5), 616-620. doi:10.1136/bjo.2005.085076
- Jiang, Y., Qi, X., Chrenek, M. A., Gardner, C., Dalal, N., Boatright, J. H., . . . Nickerson, J. M. (2014). Analysis of mouse RPE sheet morphology gives discriminatory categories. *Advances in Experimental Medicine and Biology*, 801, 601-607. doi:10.1007/978-1-4614-3209-8_76
- Joachim, N., Mitchell, P., Burlutsky, G., Kifley, A., & Wang, J. J. (2015). The Incidence and Progression of Age-Related Macular Degeneration over 15 Years: The Blue Mountains Eye Study. *Ophthalmology*, 122(12), 2482-2489. doi:10.1016/j.ophtha.2015.08.002
- Karasinska, J. M., de Haan, W., Franciosi, S., Ruddie, P., Fan, J., Kruit, J. K., . . . Hayden, M. R. (2013). ABCA1 influences neuroinflammation and neuronal death. *Neurobiology of Disease*, 54, 445-455. doi:10.1016/j.nbd.2013.01.018
- Kast, B., Schori, C., & Grimm, C. (2016). Hypoxic preconditioning protects photoreceptors against light damage independently of hypoxia inducible transcription factors in rods. *Experimental Eye Research*, 146, 60-71. doi:10.1016/j.exer.2015.12.008
- Kauppinen, A., Paterno, J. J., Blasiak, J., Salminen, A., & Kaarniranta, K. (2016). Inflammation and its role in age-related macular degeneration. *Cellular and Molecular Life Sciences*, 73(9), 1765-1786. doi:10.1007/s00018-016-2147-8
- Kiser, P. D., & Palczewski, K. (2016). Retinoids and Retinal Diseases. *Annual review of vision science*, 2, 197-234. doi:10.1146/annurev-vision-111815-114407
- Klein, R., Lee, K. E., Gangnon, R. E., & Klein, B. E. K. (2013). Incidence of visual impairment over a 20-year period: the Beaver Dam Eye Study. *Ophthalmology*, 120(6), 1210-1219. doi:10.1016/j.ophtha.2012.11.041

- Koldamova, R., Fitz, N. F., & Lefterov, I. (2014). ATP-binding cassette transporter A1: From metabolism to neurodegeneration. *Neurobiology of Disease*, 72, 13-21. doi:10.1016/j.nbd.2014.05.007
- Kruit, J. K., Wijesekara, N., Westwell-Roper, C., Vanmierlo, T., de Haan, W., Bhattacharjee, A., . . . Hayden, M. R. (2012). Loss of Both ABCA1 and ABCG1 Results in Increased Disturbances in Islet Sterol Homeostasis, Inflammation, and Impaired β -Cell Function. *Diabetes*, 61(3), 659-664. doi:10.2337/db11-1341
- Lakkaraju, A., Finnemann, S. C., & Rodriguez-Boulan, E. (2007). The lipofuscin fluorophore A2E perturbs cholesterol metabolism in retinal pigment epithelial cells. *Proceedings of the National Academy of Sciences*, 104(26), 11026-11031. doi:10.1073/pnas.0702504104
- Leach, L. L., Croze, R. H., Hu, Q., Nadar, V. P., Clevenger, T. N., Pennington, B. O., . . . Clegg, D. O. (2016). Induced Pluripotent Stem Cell-Derived Retinal Pigmented Epithelium: A Comparative Study Between Cell Lines and Differentiation Methods. *Journal of Ocular Pharmacology and Therapeutics*, 32(5), 317-330. doi:10.1089/jop.2016.0022
- Li, G., Gu, H.-M., & Zhang, D.-W. (2013). ATP-binding cassette transporters and cholesterol translocation. *IUBMB Life*, 65(6), 505-512. doi:doi:10.1002/iub.1165
- Lim, L. S., Mitchell, P., Seddon, J. M., Holz, F. G., & Wong, T. Y. (2012). Age-related macular degeneration. *The Lancet*, 379(9827), 1728-1738. doi:http://dx.doi.org/10.1016/S0140-6736(12)60282-7
- Lyssenko, N. N., Haider, N., Picataggi, A., Cipollari, E., Jiao, W., Phillips, M. C., . . . Chavali, V. R. M. (2018). Directional ABCA1-mediated cholesterol efflux and apoB-lipoprotein secretion in the retinal pigment epithelium. *Journal of Lipid Research*. doi:10.1194/jlr.M087361
- Martin, R. E., Elliott, M. H., Brush, R. S., & Anderson, R. E. (2005). Detailed Characterization of the Lipid Composition of Detergent-Resistant Membranes from Photoreceptor Rod Outer Segment Membranes. *Investigative Ophthalmology and Visual Science*, 46(4), 1147-1154. doi:10.1167/iovs.04-1207
- Masuda, T., & Esumi, N. (2010). SOX9, through Interaction with Microphthalmia-associated Transcription Factor (MITF) and OTX2, Regulates BEST1 Expression in the Retinal Pigment Epithelium. *Journal of Biological Chemistry*, 285(35), 26933-26944. doi:10.1074/jbc.M110.130294
- McVean, G. A., Altshuler, D. M., Durbin, R. M., Abecasis, G. R., Bentley, D. R., Chakravarti, A., . . . McVean, G. A. (2012). An integrated map of genetic variation from 1,092 human genomes. *Nature*, 491, 56. doi:10.1038/nature11632
- Milenkovic, A., Brandl, C., Milenkovic, V. M., Jendryke, T., Sirianant, L., Wanitchakool, P., . . . Weber, B. H. F. (2015). Bestrophin 1 is indispensable for volume regulation in human retinal pigment epithelium cells. *Proceedings of the National Academy of Sciences*, 112(20), E2630-E2639. doi:10.1073/pnas.1418840112
- Nagai, H., & Kalnins, V. I. (1996). Normally Occurring Loss of Single Cells and Repair of Resulting Defects in Retinal Pigment Epithelium In Situ. *Experimental Eye Research*, 62(1), 55-62. doi:10.1006/exer.1996.0007
- Narváez-Rivas, M., & Zhang, Q. (2016). Comprehensive untargeted lipidomic analysis using core-shell C30 particle column and high field orbitrap mass spectrometer. *Journal of Chromatography A*, 1440, 123-134. doi:10.1016/j.chroma.2016.02.054
- Oczos, J., Sutter, I., Kloeckener-Gruissem, B., Berger, W., Riwanto, M., Rentsch, K., . . . Grimm, C. (2014). Lack of paraoxonase 1 alters phospholipid composition, but not morphology and function of the mouse retina. *Investigative Ophthalmology and Visual Science*, 55(8), 4714-4727. doi:10.1167/iovs.14-14332
- Olofsson, S.-O., Boström, P., Andersson, L., Rutberg, M., Perman, J., & Borén, J. (2009). Lipid droplets as dynamic organelles connecting storage and efflux of lipids. *Biochimica et Biophysica Acta (BBA) - Molecular and Cell Biology of Lipids*, 1791(6), 448-458. doi:10.1016/j.bbalip.2008.08.001
- Owsley, C., Jackson, G. R., White, M., Feist, R., & Edwards, D. (2001). Delays in rod-mediated dark adaptation in early age-related maculopathy. *Ophthalmology*, 108(7), 1196-1202. doi:10.1016/S0161-6420(01)00580-2
- Owsley, C., McGwin Jr, G., Jackson, G. R., Kallies, K., & Clark, M. (2007). Cone- and Rod-Mediated Dark Adaptation Impairment in Age-Related Maculopathy. *Ophthalmology*, 114(9), 1728-1735. doi:10.1016/j.ophtha.2006.12.023
- Panday, N., Benz, J., Blum-Kaelin, D., Bourgeaux, V., Dehmlow, H., Hartman, P., . . . Wright, M. B. (2006). Synthesis and evaluation of anilinohexafluoroisopropanols as activators/modulators of LXR α and β . *Bioorganic & Medicinal Chemistry Letters*, 16(19), 5231-5237. doi:10.1016/j.bmcl.2006.06.081

- Pauleikhoff, D., Harper, C. A., Marshall, J., & Bird, A. C. (1990). Aging changes in Bruch's membrane. *Ophthalmology*, 97(2), 171-178. doi:http://dx.doi.org/10.1016/S0161-6420(90)32619-2
- Pellegrino, R. M., Di Veroli, A., Valeri, A., Goracci, L., & Cruciani, G. (2014). LC/MS lipid profiling from human serum: a new method for global lipid extraction. *Analytical and Bioanalytical Chemistry*, 406(30), 7937-7948. doi:10.1007/s00216-014-8255-0
- Peter, I., Huggins, G. S., Ordovas, J. M., Haan, M., & Seddon, J. M. (2011). Evaluation of new and established age-related macular degeneration susceptibility genes in the Women's Health Initiative Sight Exam (WHI-SE) Study. *American Journal of Ophthalmology*, 152(6), 1005-1013.e1001. doi:10.1016/j.ajo.2011.05.016
- Pikuleva, I. A., & Curcio, C. A. (2014). Cholesterol in the retina: the best is yet to come. *Progress in Retinal and Eye Research*, 41, 64-89. doi:10.1016/j.preteyeres.2014.03.002
- Quazi, F., & Molday, R. S. (2011). Lipid transport by mammalian ABC proteins. *Essays in Biochemistry*, 50, 265-290. doi:10.1042/bse0500265
- Rattner, A., & Nathans, J. (2006). Macular degeneration: recent advances and therapeutic opportunities. *Nat Rev Neurosci*, 7(11), 860-872. doi:10.1038/nrn2007
- Rhyne, J., Mantaring, M. M., Gardner, D. F., & Miller, M. (2009). Multiple splice defects in ABCA1 cause low HDL-C in a family with Hypoalphalipoproteinemia and premature coronary disease. *BMC Medical Genetics*, 10(1), 1. doi:10.1186/1471-2350-10-1
- Ristau, T., Ersoy, L., Lechanteur, Y., den Hollander, A. I., Daha, M. R., Hahn, M., . . . Fauser, S. (2014). Allergy Is a Protective Factor Against Age-Related Macular Degeneration. *Investigative Ophthalmology and Visual Science*, 55(1), 210-214. doi:10.1167/iov.13-13248
- Roman, D., Zhong, H., Yaklichkin, S., Chen, R., & Mardon, G. (2018). Conditional loss of Kcnj13 in the retinal pigment epithelium causes photoreceptor degeneration. *Experimental Eye Research*, 176, 219-226. doi:10.1016/j.exer.2018.07.014
- Rudolf, M., Malek, G., Messinger, J. D., Clark, M. E., Wang, L., & Curcio, C. A. (2008). Sub-retinal drusenoid deposits in human retina: Organization and composition. *Experimental Eye Research*, 87(5), 402-408. doi:10.1016/j.exer.2008.07.010
- Saari, J. C. (2012). Vitamin A Metabolism in Rod and Cone Visual Cycles. *Annual Review of Nutrition*, 32(1), 125-145. doi:10.1146/annurev-nutr-071811-150748
- Samardzija, M., von Lintig, J., Tanimoto, N., Oberhauser, V., Thiersch, M., Remé, C. E., . . . Wenzel, A. (2008). R91W mutation in Rpe65 leads to milder early-onset retinal dystrophy due to the generation of low levels of 11-cis-retinal. *Human Molecular Genetics*, 17(2), 281-292. doi:10.1093/hmg/ddm304
- Samardzija, M., Wenzel, A., Auenberg, S., Thiersch, M., Remé, C., & Grimm, C. (2006). Differential role of Jak-STAT signaling in retinal degenerations. *FASEB Journal*, 20(13), 2411-2413. doi:10.1096/fj.06-5895fje
- Sarks, S. H. (1980). Council Lecture. Drusen and their relationship to senile macular degeneration. *Australian Journal of Ophthalmology*, 8(2), 117-130.
- Schaefer, E. J., Anthanont, P., Diffenderfer, M. R., Polisecki, E., & Asztalos, B. F. (2016). Diagnosis and treatment of high density lipoprotein deficiency. *Progress in Cardiovascular Diseases*, 59(2), 97-106. doi:10.1016/j.pcad.2016.08.006
- Schultz, J. R., Tu, H., Luk, A., Repa, J. J., Medina, J. C., Li, L., . . . Shan, B. (2000). Role of LXRs in control of lipogenesis. *Genes & Development*, 14(22), 2831-2838. doi:10.1101/gad.850400
- Sene, A., Khan, Aslam A., Cox, D., Nakamura, Rei E. I., Santeford, A., Kim, Bryan M., . . . Apte, Rajendra S. (2013). Impaired cholesterol efflux in senescent macrophages promotes age-related macular degeneration. *Cell Metabolism*, 17(4), 549-561. doi:10.1016/j.cmet.2013.03.009
- Spaide, R. F., Ooto, S., & Curcio, C. A. (2018). Subretinal drusenoid deposits AKA pseudodrusen. *Survey of Ophthalmology*. doi:10.1016/j.survophthal.2018.05.005
- Storti, F., Raphael, G., Griesser, V., Klee, K., Drawnel, F., Willburger, C., . . . Maugeais, C. (2017). Regulated efflux of photoreceptor outer segment-derived cholesterol by human RPE cells. *Experimental Eye Research*, 165, 65-77. doi:10.1016/j.exer.2017.09.008
- Strauss, O. (2005). The Retinal Pigment Epithelium in Visual Function. *Physiological Reviews*, 85(3), 845-881. doi:10.1152/physrev.00021.2004
- Sundermeier, T. R., Sakami, S., Sahu, B., Howell, S. J., Gao, S., Dong, Z., . . . Palczewski, K. (2017). MicroRNA-processing Enzymes Are Essential for Survival and Function of Mature Retinal Pigmented Epithelial Cells in Mice. *The Journal of Biological Chemistry*, 292(8), 3366-3378. doi:10.1074/jbc.M116.770024
- Tabas, I. (2002). Consequences of cellular cholesterol accumulation: basic concepts and physiological implications. *The Journal of Clinical Investigation*, 110(7), 905-911. doi:10.1172/JCI16452

- Thanos, A., Morizane, Y., Murakami, Y., Giani, A., Mantopoulos, D., Kayama, M., . . . Vavvas, D. G. (2012). Evidence for Baseline Retinal Pigment Epithelium Pathology in the Trp1-Cre Mouse. *The American Journal of Pathology*, 180(5), 1917-1927. doi:10.1016/j.ajpath.2012.01.017
- Timmins, J. M., Lee, J.-Y., Boudyguina, E., Kluckman, K. D., Brunham, L. R., Mulya, A., . . . Parks, J. S. (2005). Targeted inactivation of hepatic Abca1 causes profound hypoalphalipoproteinemia and kidney hypercatabolism of apoA-I. *The Journal of Clinical Investigation*, 115(5), 1333-1342. doi:10.1172/JCI23915
- Tserentsoodol, N., Gordiyenko, N. V., Pascual, I., Lee, J. W., Fliesler, S. J., Rodriguez, I. R., & (2006). Intraretinal lipid transport is dependent on high density lipoprotein-like particles and class B scavenger receptors. *Molecular Vision*, 12, 1319-1333
- van Leeuwen, E. M., Emri, E., Merle, B. M. J., Colijn, J. M., Kersten, E., Cougnard-Gregoire, A., . . . Lengyel, I. (2018). A new perspective on lipid research in age-related macular degeneration. *Progress in Retinal and Eye Research*. doi:10.1016/j.preteyeres.2018.04.006
- Wall, F. E., Henkel, R. D., Stern, M. P., Jenson, H. B., & Moyer, M. P. (1995). An efficient method for routine epstein-barr virus immortalization of human B lymphocytes. *In Vitro Cellular & Developmental Biology - Animal*, 31(2), 156-159. doi:10.1007/bf02633976
- Wang, L., Clark, M. E., Crossman, D. K., Kojima, K., Messinger, J. D., Mobley, J. A., & Curcio, C. A. (2010). Abundant lipid and protein components of drusen. *PloS One*, 5(4), e10329. doi:10.1371/journal.pone.0010329
- Wei, H., Xun, Z., Granado, H., Wu, A., & Handa, J. T. (2016). An easy, rapid method to isolate RPE cell protein from the mouse eye. *Experimental Eye Research*, 145, 450-455. doi:10.1016/j.exer.2015.09.015
- Wenzel, A., Oberhauser, V., Pugh, E. N., Lamb, T. D., Grimm, C., Samardzija, M., . . . von Lintig, J. (2005). The Retinal G Protein-coupled Receptor (RGR) Enhances Isomerohydrolase Activity Independent of Light. *Journal of Biological Chemistry*, 280(33), 29874-29884. doi:10.1074/jbc.M503603200
- Westerterp, M., Gourion-Arsiquaud, S., Murphy, Andrew J., Shih, A., Cremers, S., Levine, Ross L., . . . Yvan-Charvet, L. (2012). Regulation of hematopoietic stem and progenitor cell mobilization by cholesterol efflux pathways. *Cell Stem Cell*, 11(2), 195-206. doi:10.1016/j.stem.2012.04.024
- Westerterp, M., Murphy, A. J., Wang, M., Pagler, T. A., Vengrenyuk, Y., Kappus, M. S., . . . Tall, A. R. (2013). Deficiency of ATP-binding cassette transporters A1 and G1 in macrophages increases inflammation and accelerates atherosclerosis in mice. *Circulation Research*, 112(11), 1456-1465. doi:10.1161/CIRCRESAHA.113.301086
- Westerterp, M., Tsuchiya, K., Tattersall, I. W., Fotakis, P., Bochem, A. E., Molusky, M. M., . . . Tall, A. R. (2016). Deficiency of ATP-Binding Cassette Transporters A1 and G1 in Endothelial Cells Accelerates Atherosclerosis in Mice. *Arteriosclerosis, Thrombosis, and Vascular Biology*, 36(7), 1328-1337. doi:10.1161/ATVBAHA.115.306670
- Winder, A. F., Alexander, R., Garner, A., Johnston, D., Vallance, D., McCreanor, G., & Frohlich, J. (1996). The pathology of cornea in Tangier disease (familial high density lipoprotein deficiency). *Journal of Clinical Pathology*, 49(5), 407-410. doi:10.1136/jcp.49.5.407
- Wong, W. L., Su, X., Li, X., Cheung, C. M. G., Klein, R., Cheng, C.-Y., & Wong, T. Y. (2014). Global prevalence of age-related macular degeneration and disease burden projection for 2020 and 2040: a systematic review and meta-analysis. *The Lancet Global Health*, 2(2), e106-e116. doi:10.1016/S2214-109X(13)70145-1
- Yang, X., Chung, J.-Y., Rai, U., & Esumi, N. (2018). Cadherins in the retinal pigment epithelium (RPE) revisited: P-cadherin is the highly dominant cadherin expressed in human and mouse RPE in vivo. *PloS One*, 13(1), e0191279. doi:10.1371/journal.pone.0191279
- Yao, J., Jia, L., Khan, N., Lin, C., Mitter, S. K., Boulton, M. E., . . . Zacks, D. N. (2015). Deletion of autophagy inducer RB1CC1 results in degeneration of the retinal pigment epithelium. *Autophagy*, 11(6), 939-953. doi:10.1080/15548627.2015.1041699
- Yu, Y., Reynolds, R., Fagerness, J., Rosner, B., Daly, M. J., & Seddon, J. M. (2011). Association of variants in the LIPC and ABCA1 genes with intermediate and large drusen and advanced age-related macular degeneration. *Investigative Ophthalmology and Visual Science*, 52(7), 4663-4670. doi:10.1167/iovs.10-7070
- Zheng, W., Mast, N., Saadane, A., & Pikuleva, I. A. (2015). Pathways of cholesterol homeostasis in mouse retina responsive to dietary and pharmacologic treatments. *Journal of Lipid Research*, 56(1), 81-97. doi:10.1194/jlr.M053439
- Zheng, W., Reem, R. E., Omarova, S., Huang, S., DiPatre, P. L., Charvet, C. D., . . . Pikuleva, I. A. (2012). Spatial distribution of the pathways of cholesterol homeostasis in human retina. *PloS One*, 7(5), e37926. doi:10.1371/journal.pone.0037926

1020 Zweifel, S. A., Imamura, Y., Spaide, T. C., Fujiwara, T., & Spaide, R. F. (2010). Prevalence and
1021 significance of subretinal drusenoid deposits (reticular pseudodrusen) in age-related macular
1022 degeneration. *Ophthalmology*, 117(9), 1775-1781. doi:10.1016/j.ophtha.2010.01.027

1023

Tables

Table 1. Mice genotypes and nomenclature.*fllox/-*: detection of floxed and excised (KO) allele in ear biopsy.

| Genotype | Name |
|--|--|
| <i>Abca1^{fllox/fllox};Abcg1^{fllox/fllox}</i> <i>Abca1^{fllox/-};Abcg1^{fllox/fllox}</i> <i>Abca1^{fllox/fllox};Abcg1^{fllox/-}</i> <i>Abca1^{fllox/-};Abcg1^{fllox/-}</i> | Cre-negative controls: Ctr |
| <i>Abca1^{fllox/fllox};Abcg1^{fllox/fllox};BEST1Cre</i> <i>Abca1^{fllox/-};Abcg1^{fllox/fllox};BEST1Cre</i> <i>Abca1^{fllox/fllox};Abcg1^{fllox/-};BEST1Cre</i> <i>Abca1^{fllox/-};Abcg1^{fllox/-};BEST1Cre</i> | RPE-specific double KOs: RPE^{ΔAbca1;Abcg1} |
| <i>Abca1^{fllox/fllox};Abcg1^{+/+};BEST1Cre</i> <i>Abca1^{fllox/-};Abcg1^{+/+};BEST1Cre</i> | RPE-specific <i>Abca1</i> single KOs: RPE^{ΔAbca1} |
| <i>Abca1^{+/+};Abcg1^{fllox/fllox};BEST1Cre</i> <i>Abca1^{+/+};Abcg1^{fllox/-};BEST1Cre</i> | RPE-specific <i>Abcg1</i> single KOs: RPE^{ΔAbcg1} |
| <i>Abca1^{+/+};Abcg1^{+/+};BEST1Cre</i> | Cre-positive controls: BEST1Cre |

Table 2. LCLs and genotypes of the AMD-associated SNPs in human *ABCA1* intron 2.

| LCL | SNP | Genotype |
|-----------------------------|------------------|-----------|
| <i>Decreased risk</i> (n=3) | <i>rs1883025</i> | TT |
| | <i>rs2740488</i> | CC |
| <i>Increased risk</i> (n=3) | <i>rs1883025</i> | CC |
| | <i>rs2740488</i> | AA |

Figure Legends

Figure 1. Generation of RPE^{ΔAbca1;Abcg1} mice.

(A) IF staining for ABCA1 (yellow), ABCG1 (violet) and the RPE apical marker EZR (white) in retinas of 2-months-old wt mice. Lower panels show magnification of the RPE layer. Nuclei were counterstained with DAPI (blue). Ch: choroid; RPE: retinal pigment epithelium; ONL: outer nuclear layer; INL: inner nuclear layer; GCL: ganglion cell layer. **(B)** Cre mRNA levels were measured by semi-quantitative real-time PCR in neural retinas and eyecups (RPE/choroid) from 2-months-old RPE^{ΔAbca1;Abcg1} mice. Shown are data from individual samples and means ± standard deviations (SD, N=4). Statistics: Student's t-test; ***: p<0.001. **(C)** IF staining for CRE (red) in retinal sections from 2-months-old Ctr and RPE^{ΔAbca1;Abcg1} mice: white arrowheads indicate CRE-positive nuclei in the RPE of mutant mice. Nuclei were counterstained with DAPI (blue). Note the non-specific signal in the inner retina. Representative pictures of N=6 mice. **(D)** Detection of CRE-mediated excision fragments in *Abca1* and *Abcg1* (*Abca1/Abcg1* exc) by conventional PCR on genomic DNA from eyecups and neural retinas of Ctr and RPE^{ΔAbca1;Abcg1} mice (N=3). For this picture, animals showing heterozygous deletion of *Abca1/Abcg1* in ear biopsies (see "Materials and methods") were excluded in order to detect excision truly due to CRE expression in the eye. PCR for the floxed sequences (*Abca1/Abcg1* flox) was performed as positive control. Shown are PCR products run on a 2% agarose gel and visualized with ethidium bromide. Note the lack of the excised fragment in the neural retina. M: DNA size marker, indicated fragment sizes are shown in base pairs (bp).

Figure 2. Early morphological alterations and intracellular lipid accumulation in RPE^{ΔAbca1;Abcg1} mice.

(A) Fundus imaging of 2-months-old Ctr and RPE^{ΔAbca1;Abcg1} mice showing altered pigmentation pattern in mutant mice. Corresponding retinal morphology analyzed by light **(B)** and electron **(C)** microscopy revealed alterations of the RPE in RPE^{ΔAbca1;Abcg1} mice. Yellow lines in **(B)** indicate RPE borders. Yellow arrowheads in **(C)** indicate lipid droplets. OS: outer segments; N: nucleus. **(D)** Retinal sections were stained with ORO (red, dye for neutral lipids); nuclei were counterstained with hematoxylin (blue). RPE flat mounts were stained with LipidTOX (red, dye for neutral lipids) and anti-CRE (green) **(E)** or anti-CRE (red) and phalloidin (green, staining actin filaments) **(F)**. Nuclei were counterstained with Hoechst. White arrowheads indicate CRE-positive cells showing lipid accumulation in mutant mice. Representative pictures of N ≥ 3 animals per group. Abbreviations as in figure 1.

Figure 3. Effect of lipid accumulation in the ageing mouse RPE.

(A) RPE flat mounts from 4-months-old Ctr and RPE ^{$\Delta Abca1; Abcg1$} mice were stained for ZO-1 (red) and β -cat (green). White arrowheads indicate loss of co-localization between ZO-1 and β -cat in mutant RPE. Nuclei were counterstained with Hoechst. Shown are representative images of N=3 animals per group. Quantification of cell area **(B)** and cell shape **(C)** was performed using ImageJ on images from ZO-1 stained flat mounts. Corresponding measurements of single analyzed cell can be found in figure 3 - Source Data 1. Statistics: Mann-Whitney test; **: $p < 0.01$, ****: $p < 0.0001$. Light microscopy was used to visualize outer retinas of control and RPE ^{$\Delta Abca1; Abcg1$} mice: shown are panoramas **(D)** and RPE at higher magnification **(E)**. Representative images of N ≥ 3 animals per group. *Cre* **(F)** and *Mct3* **(G)** mRNA levels were measured by semi-quantitative real-time PCR in eyecups from Ctr and RPE ^{$\Delta Abca1; Abcg1$} mice at the indicated ages. Shown are data from individual samples and means \pm SD (N=3-4). Statistics: one-way ANOVA vs "2 months" of the respective genotype; *: $p < 0.05$, ***: $p < 0.001$. n.d.: not detected. Abbreviations as in figure 1.

Figure 4. Lipid accumulation after AAV-mediated excision of *Abca1* and *Abcg1* in adult RPE.

(A) Schematic representation of the vector packaged into AAV4 capsid in order to express *Cre* and *GFP* specifically in the RPE of *Abca1*^{*fllox/fllox*}; *Abcg1*^{*fllox/fllox*} mice. Length of the construct in base pairs is shown below the map. ITR: inverted terminal repeat; SV40 SD/SA: simian virus 40 splice donor/splice acceptor site; P2A: porcine teschovirus 2A; bGH polyA: bovine growth hormone polyadenylation tail. 10 weeks after sub-retinal injections, co-localization of AAV-mediated *Cre/GFP* expression and lipid accumulation was analyzed by IF in RPE flat mounts **(B)** and retinal sections **(C-F)**. **(B)** RPE flat mounts were stained with LipidTOX (red); shown are representative images of a non-transduced and a transduced area. Dorsal-ventral retinal sections were stained with ORO: retina panorama is shown in **(C)** and magnified images of a non-transduced and a transduced area (corresponding to yellow and red rectangles in the panorama) are shown in **(D)**. Yellow arrowhead indicates LDs in the transduced RPE. Nuclei were counterstained with hematoxylin (blue). Consecutive retinal sections were analyzed for AAV transduction by IF: retinal panorama is shown in **(E)** and magnified pictures of a non-transduced and a transduced area (corresponding to yellow and red rectangles in the panorama) are shown in **(F)**, together with CRE staining. White arrowheads indicate CRE-positive nuclei in the transduced RPE. Black **(C)** and white **(E)** arrows indicate the injection site. Nuclei were counterstained with DAPI (blue). Representative pictures of N ≥ 3 animals per group. Abbreviations as in figure 1.

Figure 5. Cholesteryl esters as main components of LDs in the RPE of RPE^{ΔAbca1;Abcg1} mice.

Lipid composition of eyecups (**A**), neural retinas (**C**) and plasma (**D**) from 2-months-old Ctr and mutant mice was measured by mass spectrometry-based methods. The following lipid classes were analyzed: cholesterol (un-esterified cholesterol, UC, and cholesteryl esters, CEs), phospholipids (PLs: sum of phosphatidylcholine, phosphatidylethanolamine, phosphatidylserine, phosphatidylinositol and phosphatidylglycerol), sphingolipids (SLs: ceramides, Cer, and sphingomyelins, SMs) and glycerolipids (GLs: diacylglycerols, DAGs, and triglycerides, TGs). (**B**) Cholesteryl esters species containing the indicated fatty acids were quantified in eyecups from the same animals. (**E**) Relative quantification of retinyl esters was performed in eyecups from 2-months-old Ctr and RPE^{ΔAbca1;Abcg1} mice. Shown are box plots of folds on respective Ctr average, whiskers correspond to min and max values (N=4-10). Lipid concentration values corresponding to fold changes in (**A**), (**C**) and (**D**) as well as single PL classes can be found in supplementary table S1. Please note that UC, CEs and REs were determined in RPE-enriched eyecups whereas PLs, SLs and GLs were determined in whole eyecups. Also, tissues from both eyes of the same animals were used for analysis of UC, CEs and REs, whereas tissues from single eyes were used for PLs, SLs and GLs (see “Materials and methods”). Statistics: Student’s t-test vs “Ctr”; *: p<0.05, **: p<0.01, ***: p<0.001.

Figure 6. Delayed RHO regeneration in RPE^{ΔAbca1;Abcg1} mice.

Dark-adapted 2-months-old Ctr and RPE^{ΔAbca1;Abcg1} mice were exposed to 5'000 lux for 10 min and the RHO content was measured in each retina. Dark controls were kept in darkness for the entire procedure. RHO levels were measured in dark controls, immediately after bleach (0 min) and after 30, 60 and 120 min of recovery in darkness. (**A**) “Total” amount of regenerated RHO after 120 min was calculated by subtracting the corresponding averaged RHO amount at “0 min” from the RHO levels at “120 min”. (**B**) Amount of regenerated RHO during the indicated time intervals after bleaching were calculated by subtracting the corresponding averaged RHO amount at the early time point from the RHO levels measured at the later time point. Shown are data from individual samples and means ± SD (N=4-8 eyes, corresponding to 2-4 mice). Statistics: Student’s t-test vs “Ctr”; *: p<0.05. Averages and SD of RHO content measurements can be found in supplementary table S2; single measurements per eye can be found in Figure 6 - Source Data 1.

Figure 7. Age-dependent retinal degeneration in RPE^{ΔAbca1;Abcg1} mice.

(A) Fundus images (upper panels) and OCT scans (lower panels, corresponding to red lines in fundus) of Ctr and RPE^{ΔAbca1;Abcg1} mice at the indicated age. White arrowheads indicate sub-retinal hyper-reflective foci. Retinal morphology of the same animals was analyzed by light microscopy (B). Representative pictures of N ≥ 3 animals per group. ONL thickness was quantified from nasal-temporal panorama images at 2 and 6 months of age and presented as spidergrams (C): significant ONL thinning was detected in 6-months-old RPE^{ΔAbca1;Abcg1} mice. Shown are means ± SD (N ≥ 3). Statistics: two-way ANOVA with Sidak's multiple comparison test; *: p<0.05, **: p<0.01, ****: p<0.0001. Abbreviations as in figure 1.

Figure 8. Decreased retinal function in aged RPE^{ΔAbca1;Abcg1} mice.

Scotopic and photopic ERGs were recorded with increasing light intensities from dark-adapted Ctr and RPE^{ΔAbca1;Abcg1} mice at the indicated ages. Shown are mean ± SD (N=3-6) of scotopic a- (A) and b-wave (B) amplitudes as well as photopic b-wave (C) amplitudes. Average scotopic and photopic traces of 6-months-old animals are shown in (D) and (E), respectively. Statistics: two-way ANOVA with Sidak's multiple comparison test; *: p<0.05, +: p<0.01, #: p<0.001, §: p<0.0001.

Figure 9. Inflammatory response in RPE^{ΔAbca1;Abcg1} mice.

(A) RPE flat mounts from 4-months-old Ctr and RPE^{ΔAbca1;Abcg1} mice were stained with phalloidin (green, staining actin filaments) and anti-IBA-1 (red). Shown are representative top-view images and cross-sections (A = apical side, B = basal side). White arrowheads indicate IBA-1-positive cells located inside or at the choroidal (basal) side of the mutant RPE. Nuclei were counterstained with Hoechst. (B) Retinal sections from 6-months-old mice were stained for IBA-1 (red): increased signal intensity and presence of sub-retinal macrophages/microglia was detected in RPE^{ΔAbca1;Abcg1} mice (higher magnification images of the outer retina are shown in right panels). Nuclei were counterstained with DAPI. Representative images of N=3 animals per group. *Ilf1b* (C), *Casp1* (D) and *Gfap* (E) mRNA levels were measured by semi-quantitative real-time PCR in neural retinas from Ctr and RPE^{ΔAbca1;Abcg1} mice. Shown are data from individual samples and means ± SD (N=3-4). Statistics: one-way ANOVA vs "2 months" of the respective genotype; *: p<0.05, ****: p<0.0001. Abbreviations as in figure 1.

Figure 10. Early lipid accumulation in the RPE of single *Abca1*, but not *Abcg1*, KO mice.

2-months-old Ctr, double KO and single KO retinal sections were analyzed by light microscopy **(A)**, ORO staining **(B)** and CRE IF **(C)**. Single *Abca1* mutant mice ($RPE^{\Delta Abca1}$) showed an RPE phenotype comparable to double mutants ($RPE^{\Delta Abca1; Abcg1}$), while single *Abcg1* KO mice ($RPE^{\Delta Abcg1}$) were undistinguishable from controls. Yellow lines in **(A)** indicate RPE borders. Nuclei were counterstained with hematoxylin **(B)** or DAPI **(C)**. Representative pictures of $N \geq 3$ animals per group. Abbreviations as in figure 1.

Figure 11. ABCA1 expression in human LCLs.

LCLs derived from healthy individuals carrying the AMD decreased or increased risk *ABCA1* genotypes were stimulated with an LXR agonist (1 μ M) or DMSO vehicle control for 24 h. **(A)** *ABCA1* mRNA levels were measured by semi-quantitative real-time PCR. Shown are data from individual samples and means \pm SD ($N=3$, 3 technical replicates per cell line). Statistics: two-way ANOVA with Sidak's multiple comparison test; *: $p<0.05$. *ABCA1* protein levels were measured in LXR-stimulated cells by WB and normalized on ACTB levels. Shown are a representative WB **(B)** and the means \pm SD of the band intensity quantification ($N=3$, 5 technical replicates per cell line) **(C)**. Statistics: Student's t-test vs "decreased risk".

Figure Supplement Legends

Figure 1-figure supplement 1. Genotyping and definition of the mouse models.

(A) PCRs for *Cre* transgene, *Abca1* floxed (*flox*) and excised (*exc*) alleles, and *Abcg1* floxed and excised alleles were performed on genomic DNA extracted from eyecups and neural retinas of 2-months-old Ctr and RPE ^{$\Delta Abca1;Abcg1$} mice. Shown are PCR products run on a 2% agarose gel and visualized with ethidium bromide. Same results as for the neural retinas were obtained using ear biopsies (not shown), suggesting occasional presence of heterozygous systemic excision of *Abca1* and *Abcg1* floxed sequences. Definition of the genotypes is shown below the gel images (N=3 per group). See table 1 for definition of strain names based on the genotype. (B) *Abca1* and *Abcg1* mRNA levels were measured by semi-quantitative real-time PCR in neural retinas of 2-months-old *flox/flox* and *flox/-* mice. Shown are data from individual samples and means \pm range of the fold change on *flox/flox* genotype average (N=2-5). (C) Retinal morphology of 6-months-old *Abca1^{flox/flox};Abcg1^{flox/flox}* and *Abca1^{flox/-};Abcg1^{flox/-}* mice. Lower panels show higher magnification images of the RPE. Shown are representative images of N=3 animals per group. Abbreviations as in figure 1.

Figure 1-figure supplement 2. Gene expression in eyecups of Ctr and RPE ^{$\Delta Abca1;Abcg1$} mice.

Abca1 (A), *Abcg1* (B), *Cre* (C) and *Mct3* (D) mRNA levels were measured by semi-quantitative real-time PCR in eyecups of 2-months-old Ctr and RPE ^{$\Delta Abca1;Abcg1$} mice. Shown are data from individual samples and means \pm SD (N=3-4). n.d.: not detected.

Figure 3-figure supplement 1. *Cre* expression in RPE ^{$\Delta Abca1;Abcg1$} and *BEST1Cre* mice.

Cre mRNA levels were measured by semi-quantitative real-time PCR in eyecups of 2- and 6-months-old RPE ^{$\Delta Abca1;Abcg1$} and *BEST1Cre* mice. Shown are data from individual samples and means \pm SD (N=3-4). Statistics: Student's t-test vs "2 months" of the respective genotype; **: $p < 0.01$.

Figure 3-figure supplement 2. Absence of retinal phenotype in *BEST1Cre* mice up to 6 months of age.

(A) Retinal morphology was analyzed by light microscopy in 2- and 6-months-old *BEST1Cre* animals. Yellow arrowhead indicates an example of occasionally observed minor alterations in the RPE. Retinal sections of *BEST1Cre* mice at indicated ages were stained for lipids (B) and CRE (C). Nuclei were

counterstained with hematoxylin **(B)** or DAPI **(C)**. **(D)** Occasional bright spots were observed in the fundus of *BEST1Cre* mice (indicated by white arrowheads). Representative images of $N \geq 3$ animals per group. **(E)** ERG recordings of *BEST1Cre* and age-matched wild type animals. Shown are means \pm SD ($N=3-9$) of scotopic b-wave amplitudes. Abbreviations as in figure 1.

Figure 7-figure supplement 1. Absence of a phenotype in the inner retina of RPE ^{$\Delta Abca1; Abcg1$} mice at 6 months of age.

(A) INL thickness was quantified from nasal-temporal panorama images at 6 months of age and presented as spidergram. Shown are means \pm SD ($N \geq 3$). Statistics: two-way ANOVA with Sidak's multiple comparison test. **(B)**. Retinal sections from 6-months-old Ctr (upper panel) and RPE ^{$\Delta Abca1; Abcg1$} (lower panel) mice were stained for POU4F1 (red); nuclei were counterstained with DAPI. Note that the used secondary antibody was an anti-mouse and stained retinal blood vessels as well. Representative images of $N=3$ animals per group. GCL: ganglion cell layer.

1216 **List of supplementary and source data files:**

1217

1218 **Storti_SupplementaryFile1**

1219 Contains supplementary tables S1-S4.

1220

1221 **Figure 3 - Source Data 1**

1222 **Figure 6 - Source Data 1**

1223

1224 **Figure 1-figure supplement 1**

1225 **Figure 1-figure supplement 2**

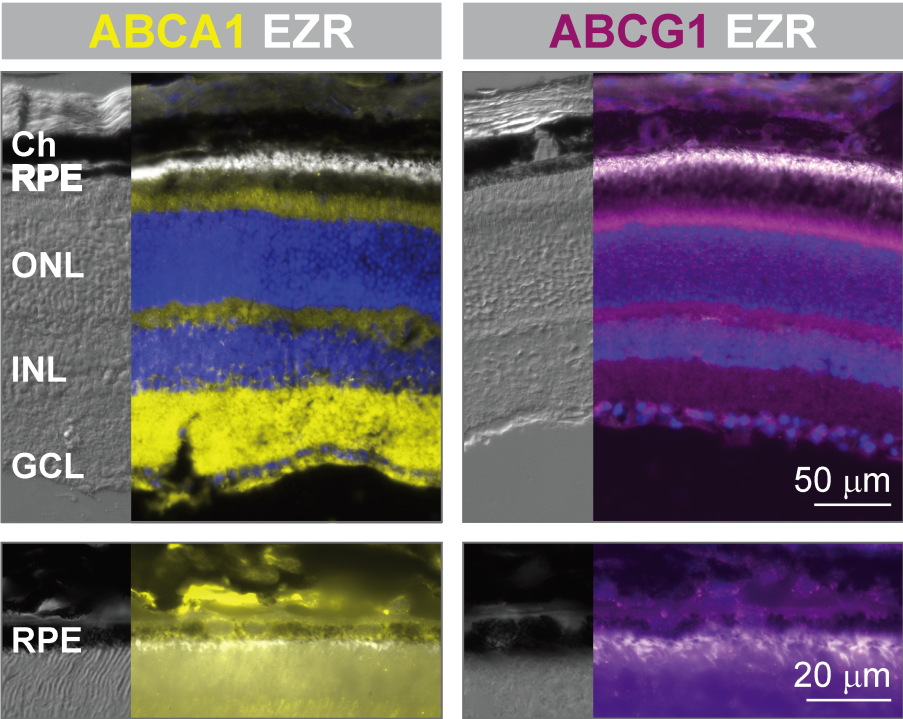
1226 **Figure 3-figure supplement 1**

1227 **Figure 3-figure supplement 2**

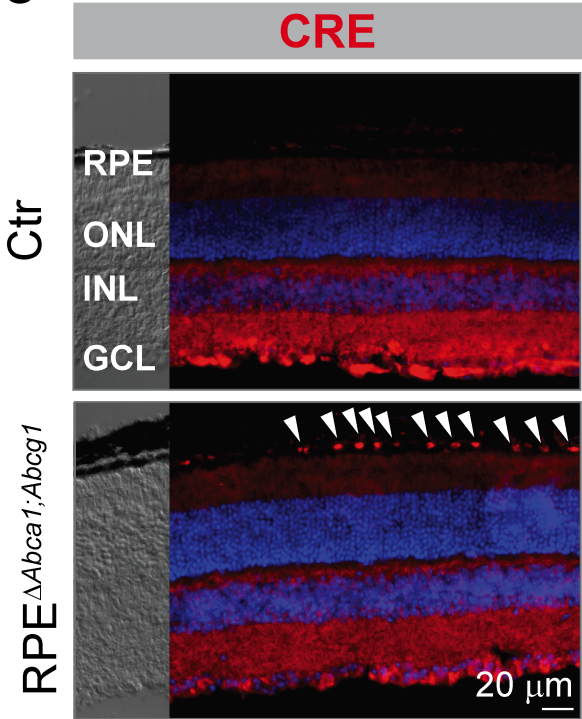
1228 **Figure 7-figure supplement 1**

Figure 1

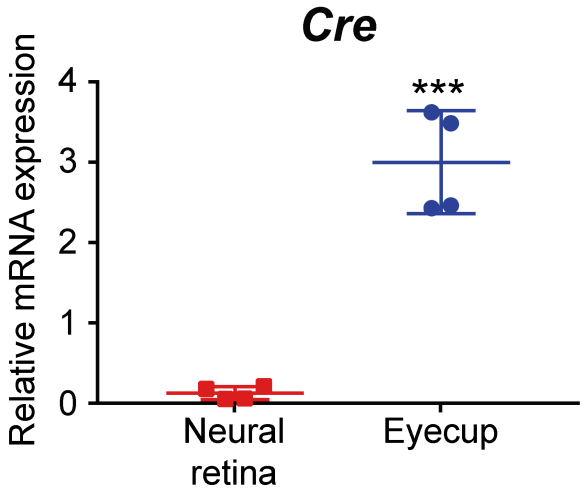
A



C



B



D

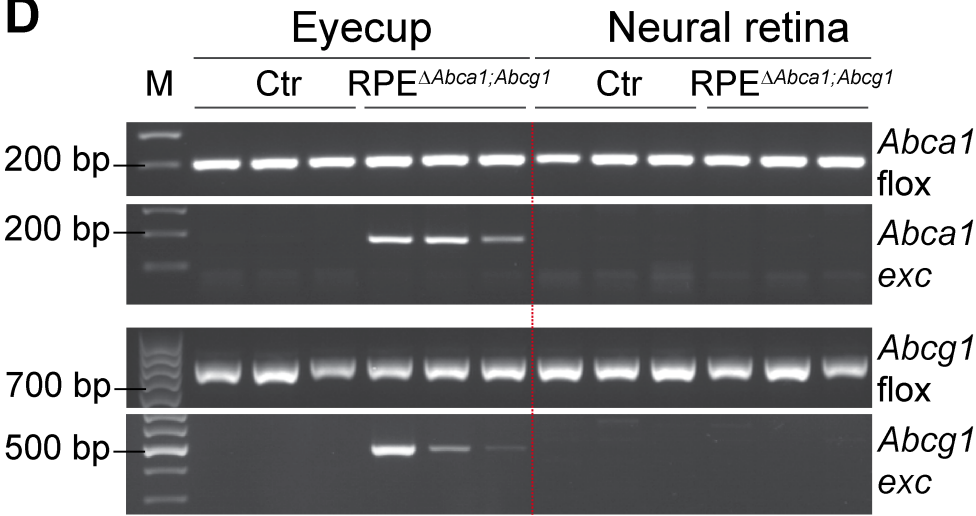


Figure 2

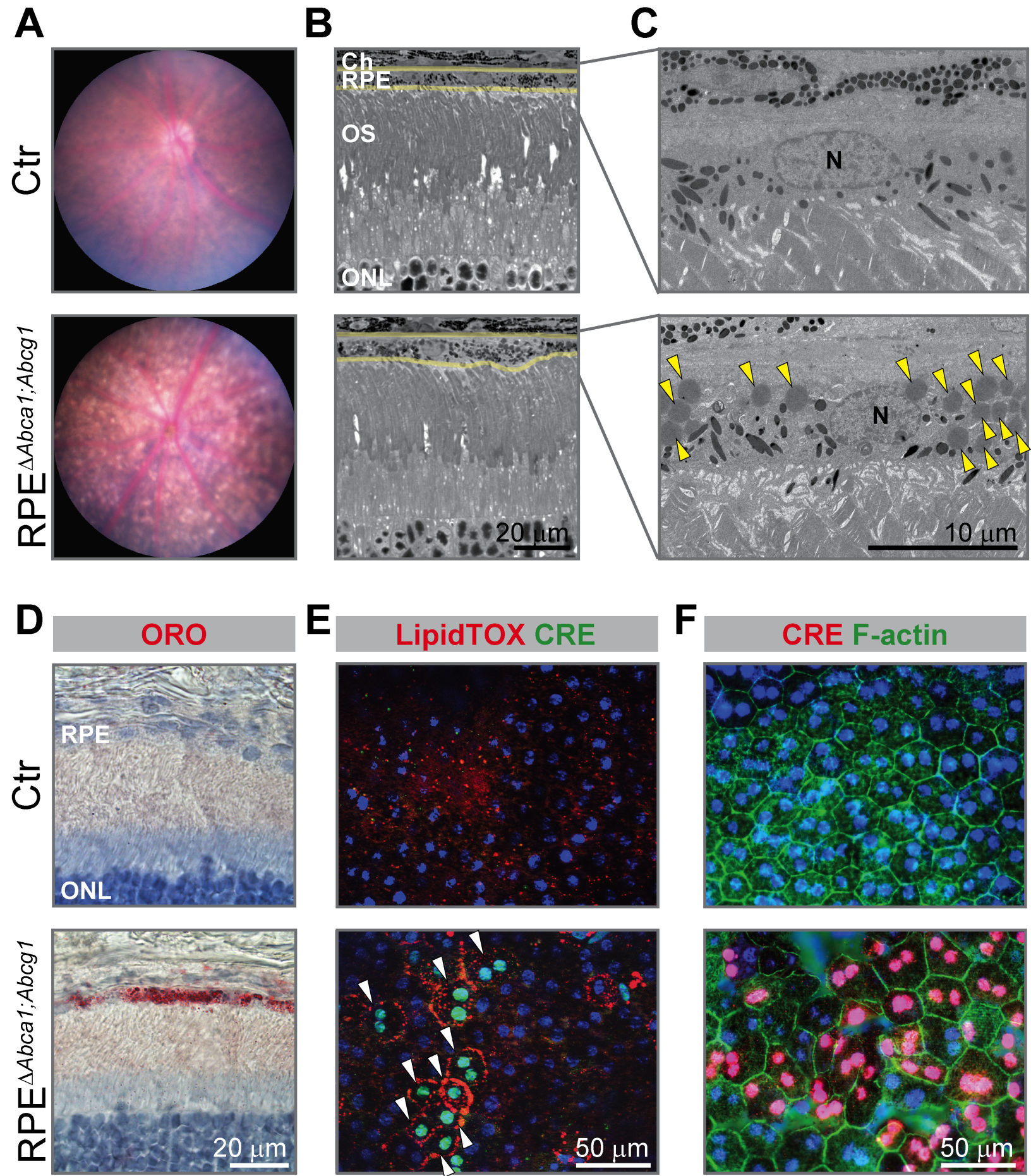


Figure 3

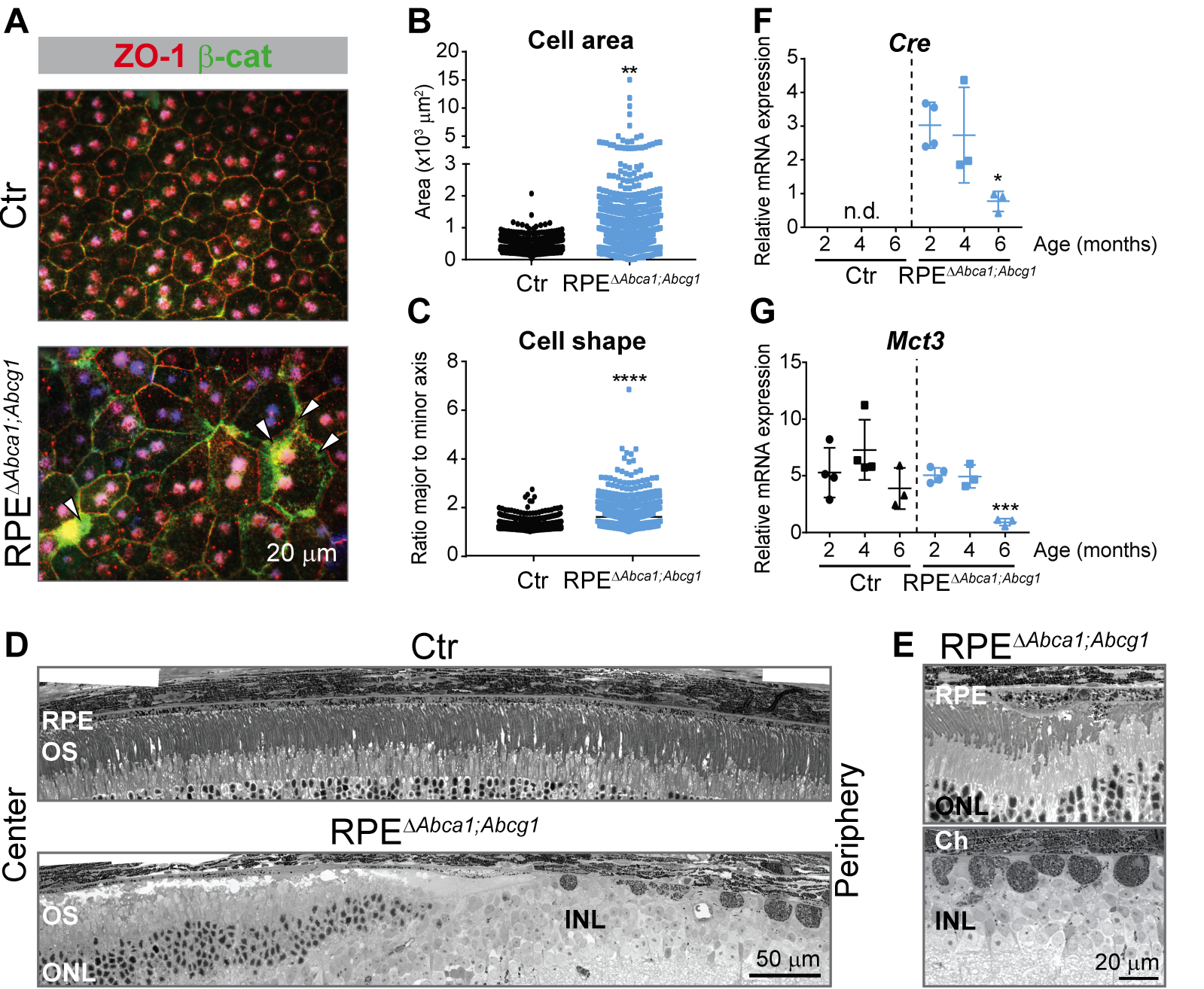
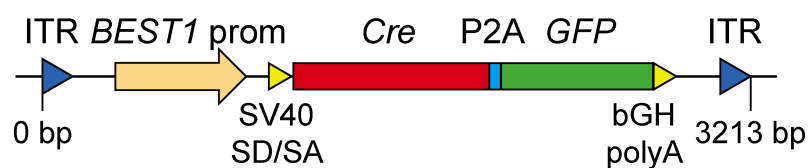
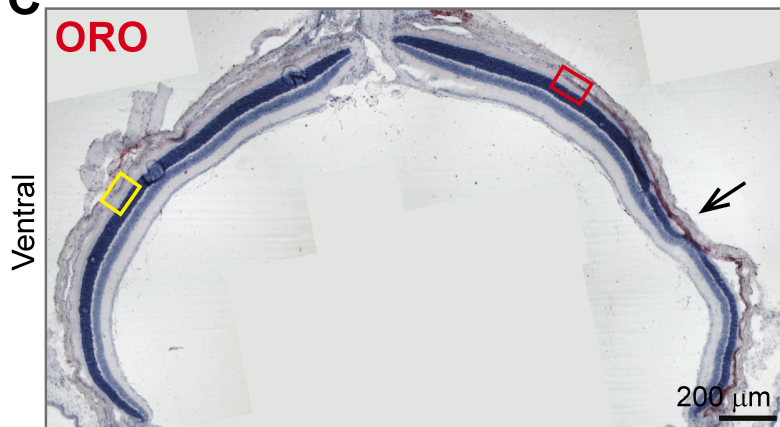


Figure 4

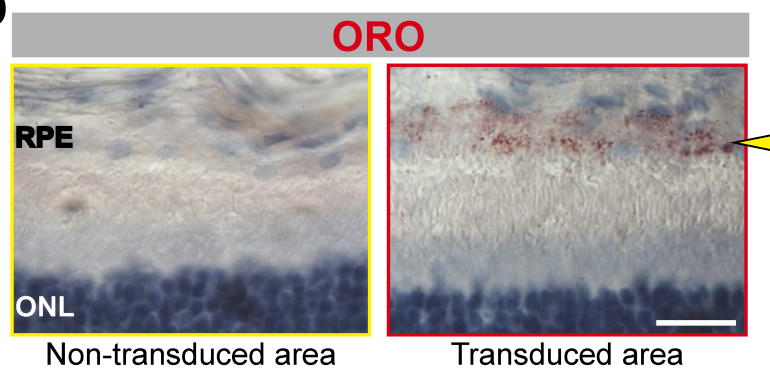
A



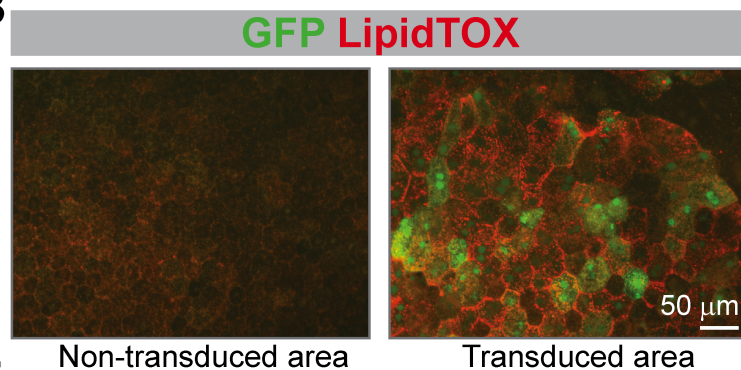
C



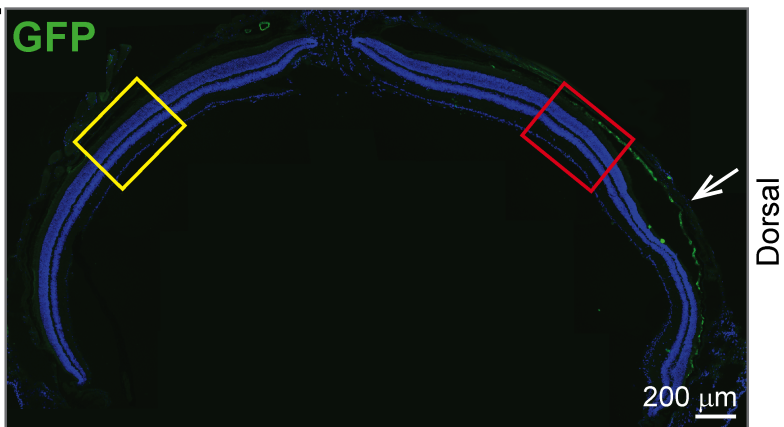
D



B



E



F

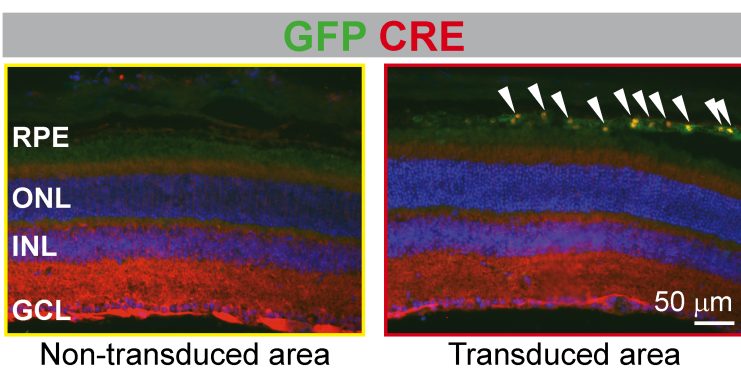


Figure 5

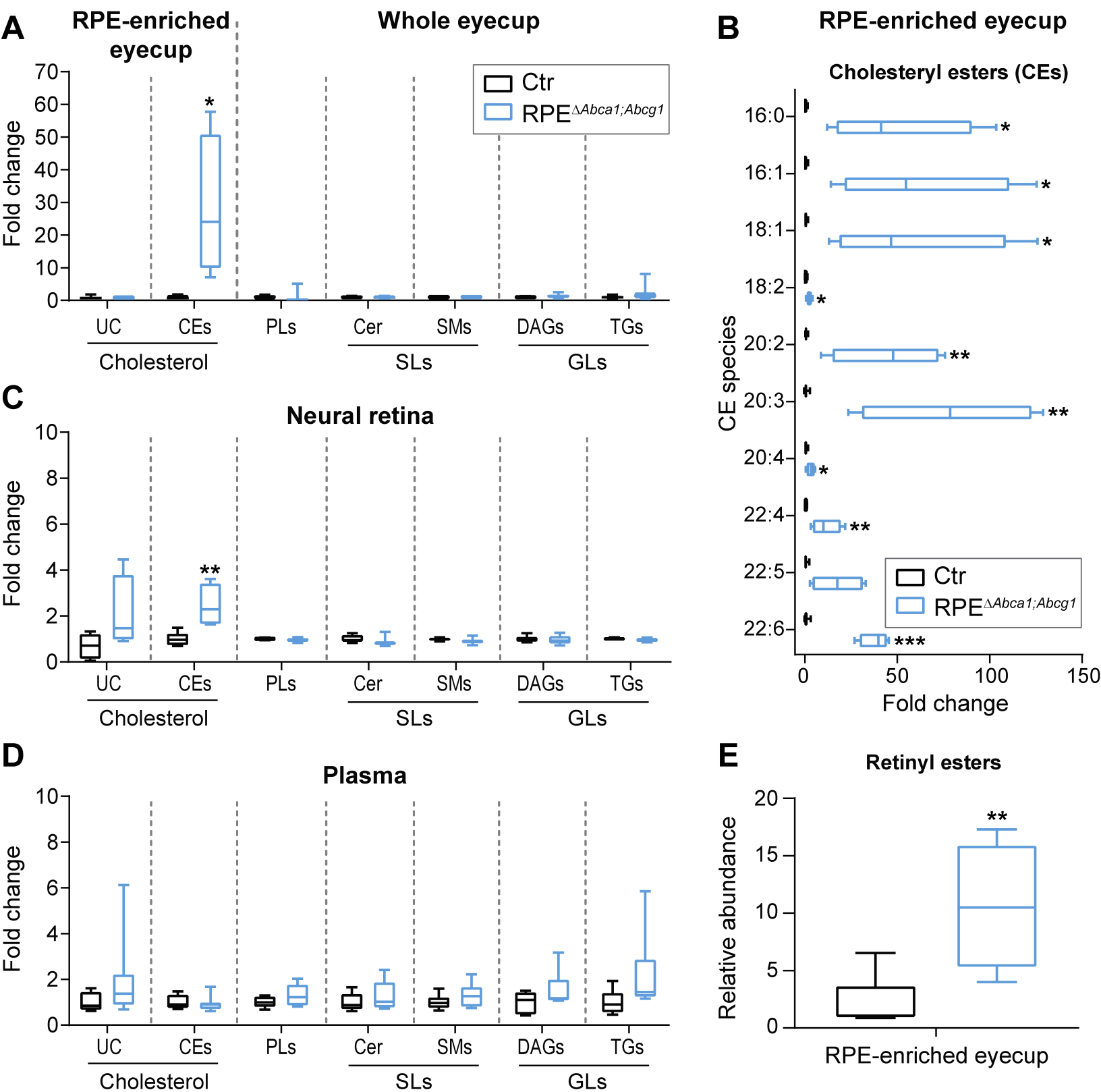


Figure 6

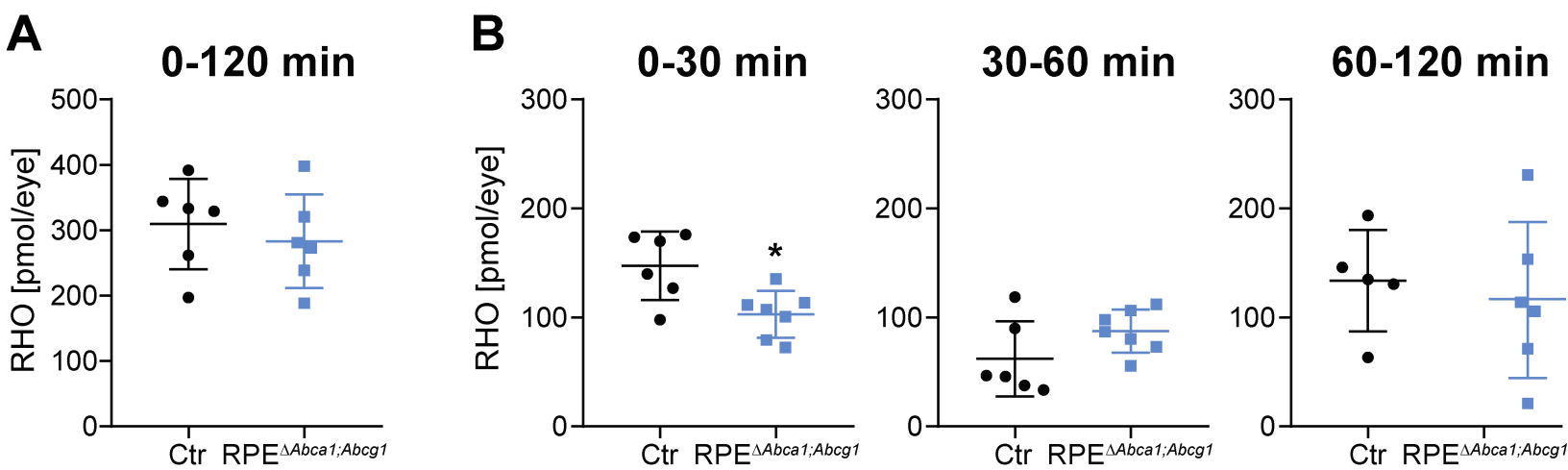


Figure 7

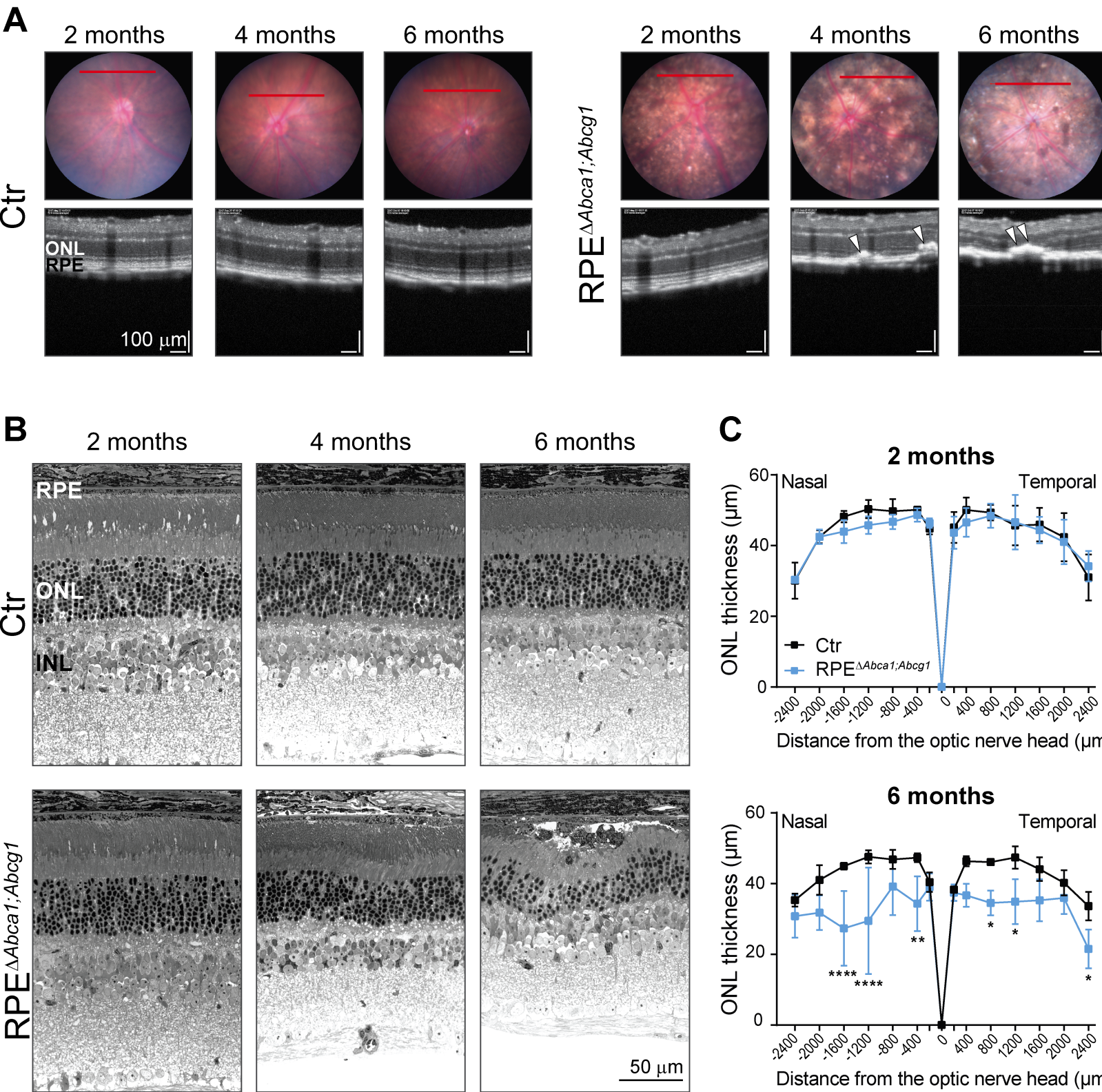


Figure 8

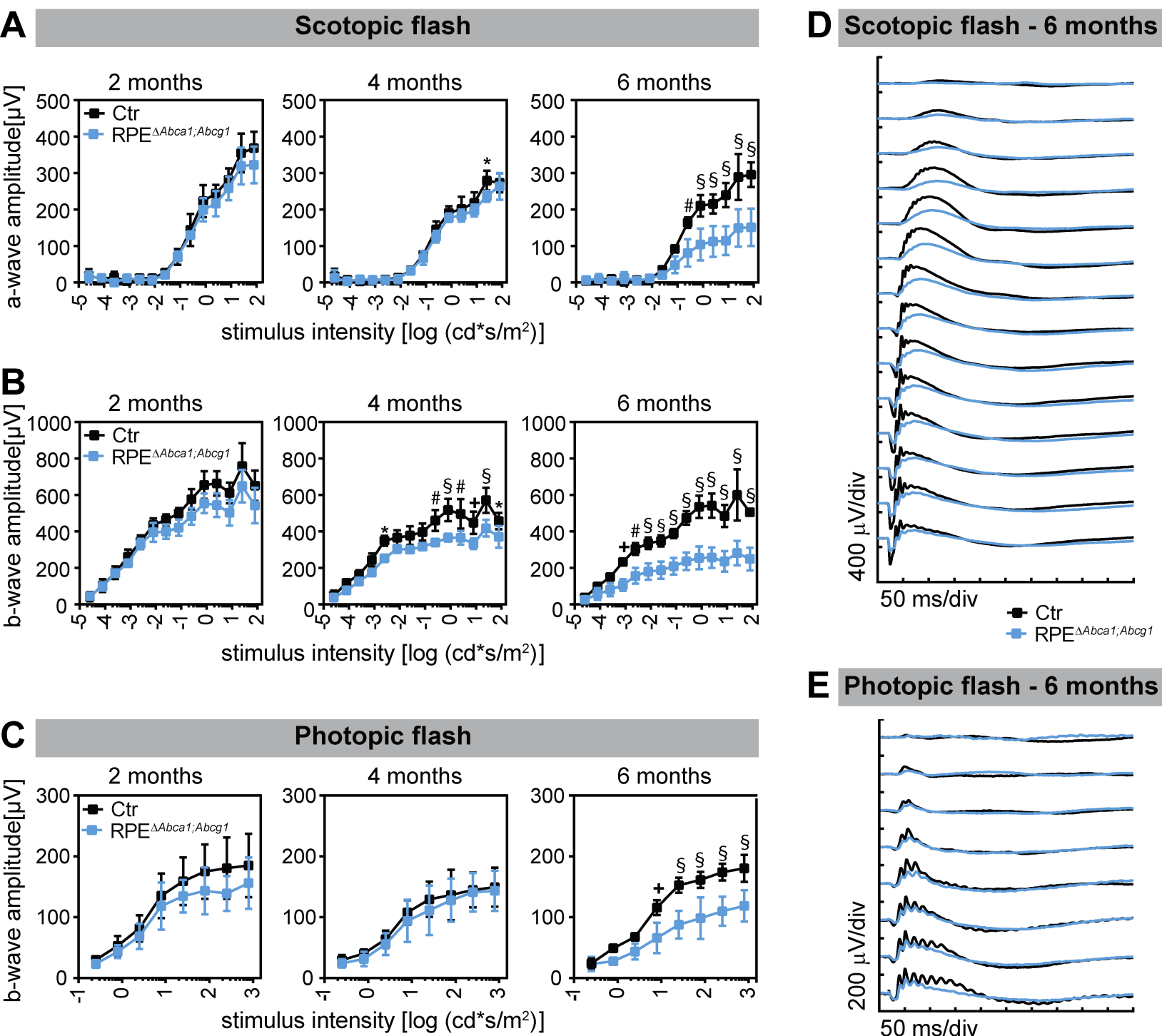


Figure 9

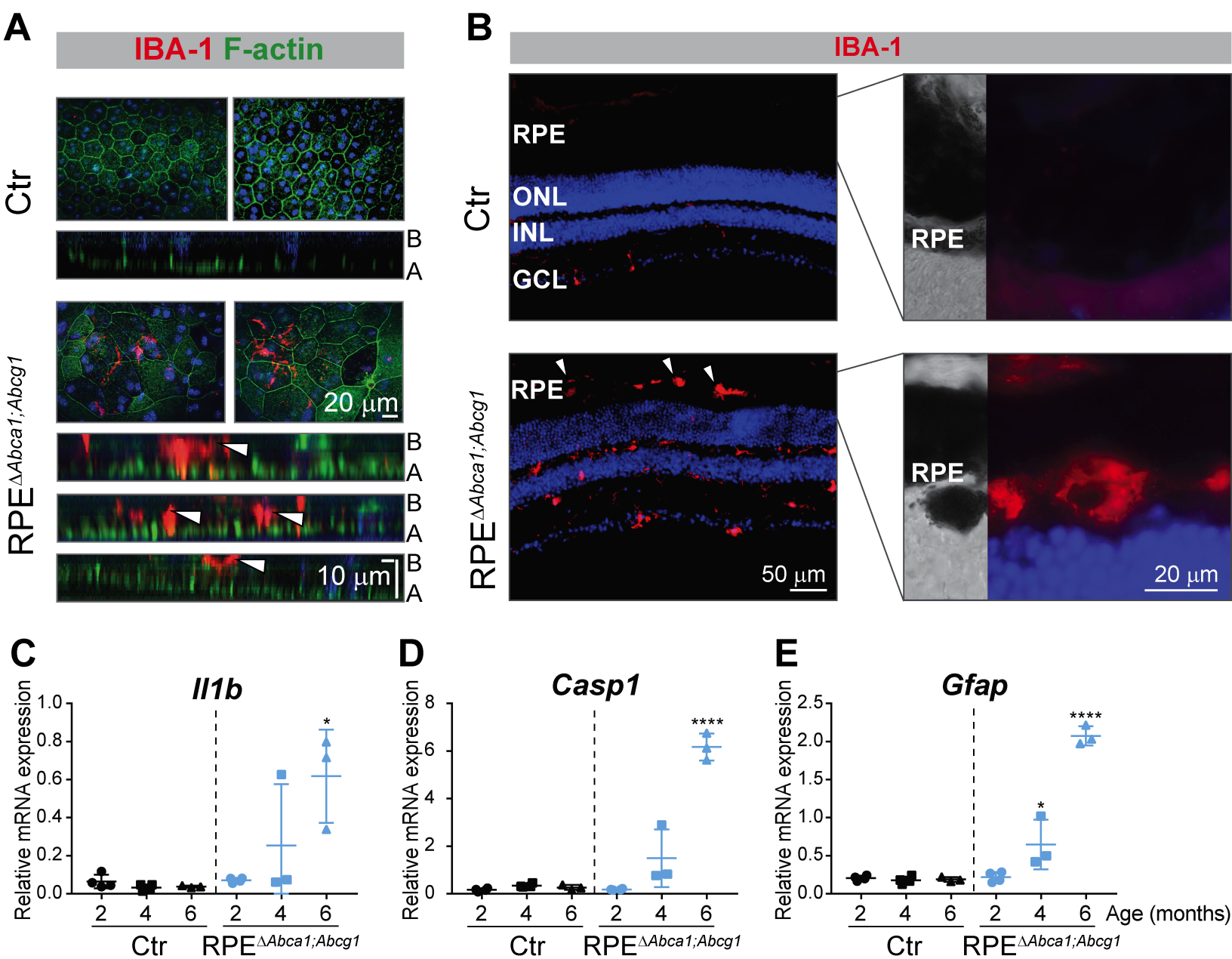


Figure 10

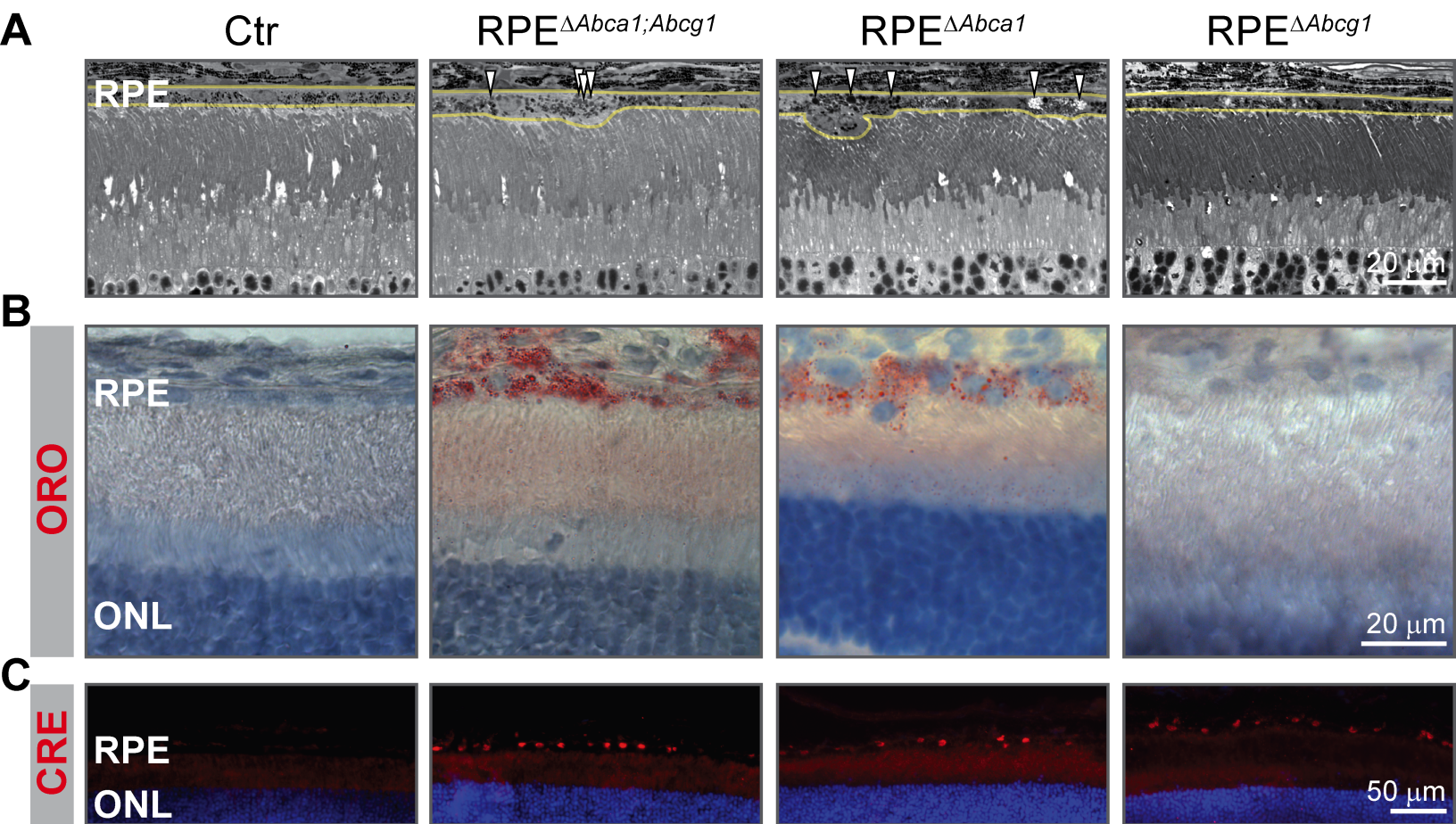


Figure 11

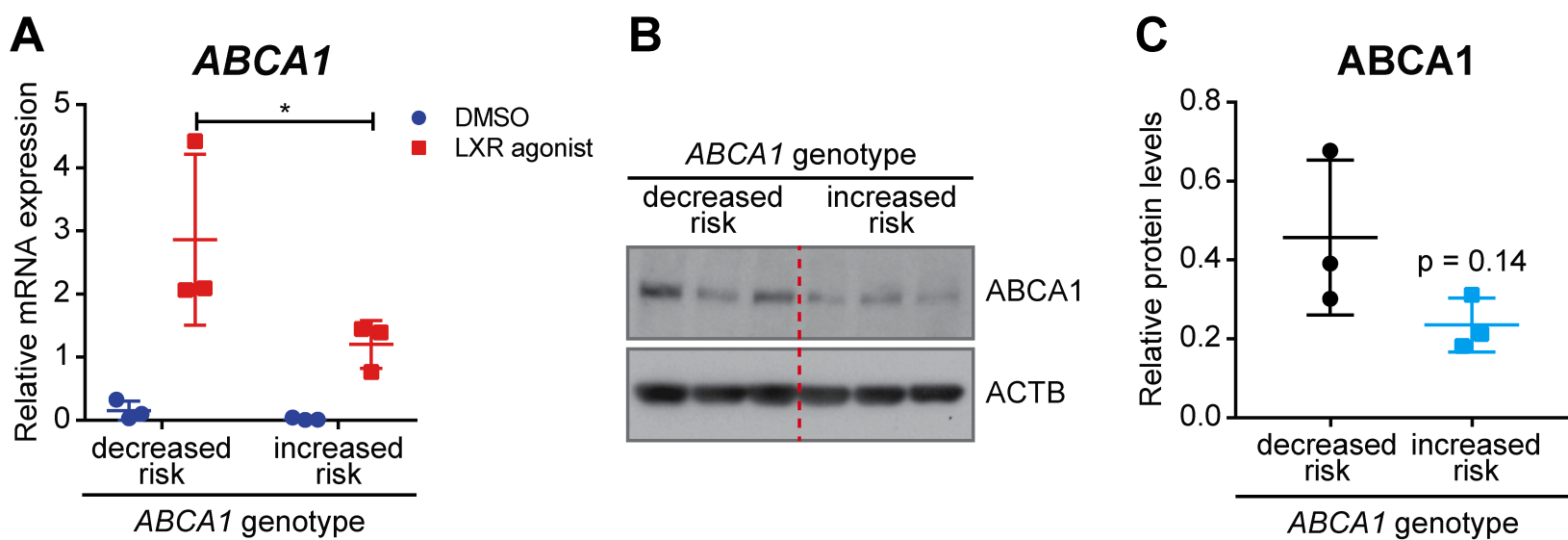
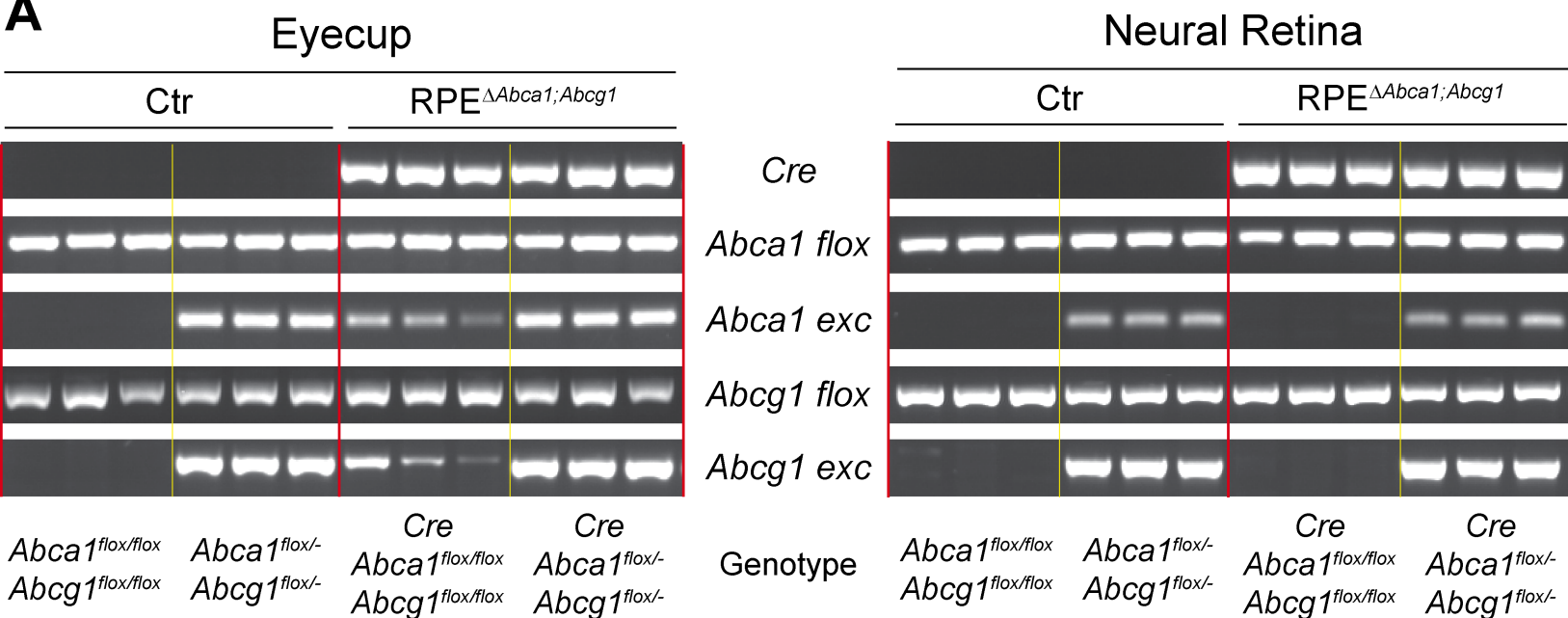
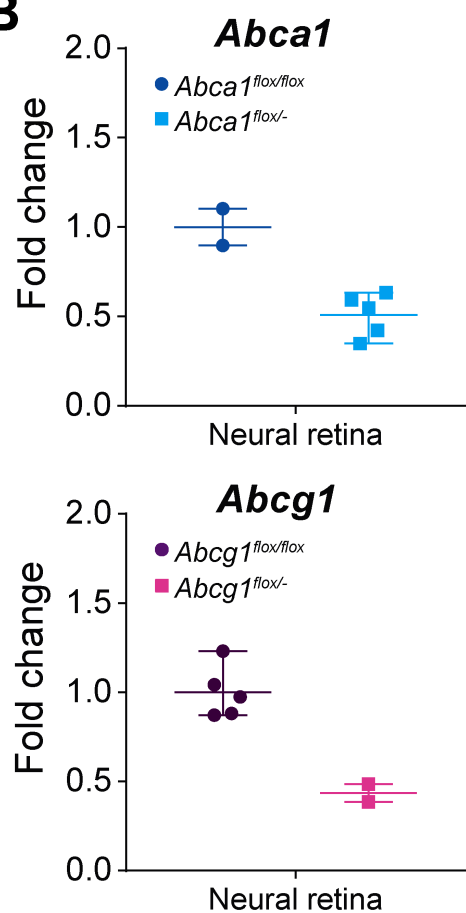


Figure 1 - Figure Supplement 1

A



B



C

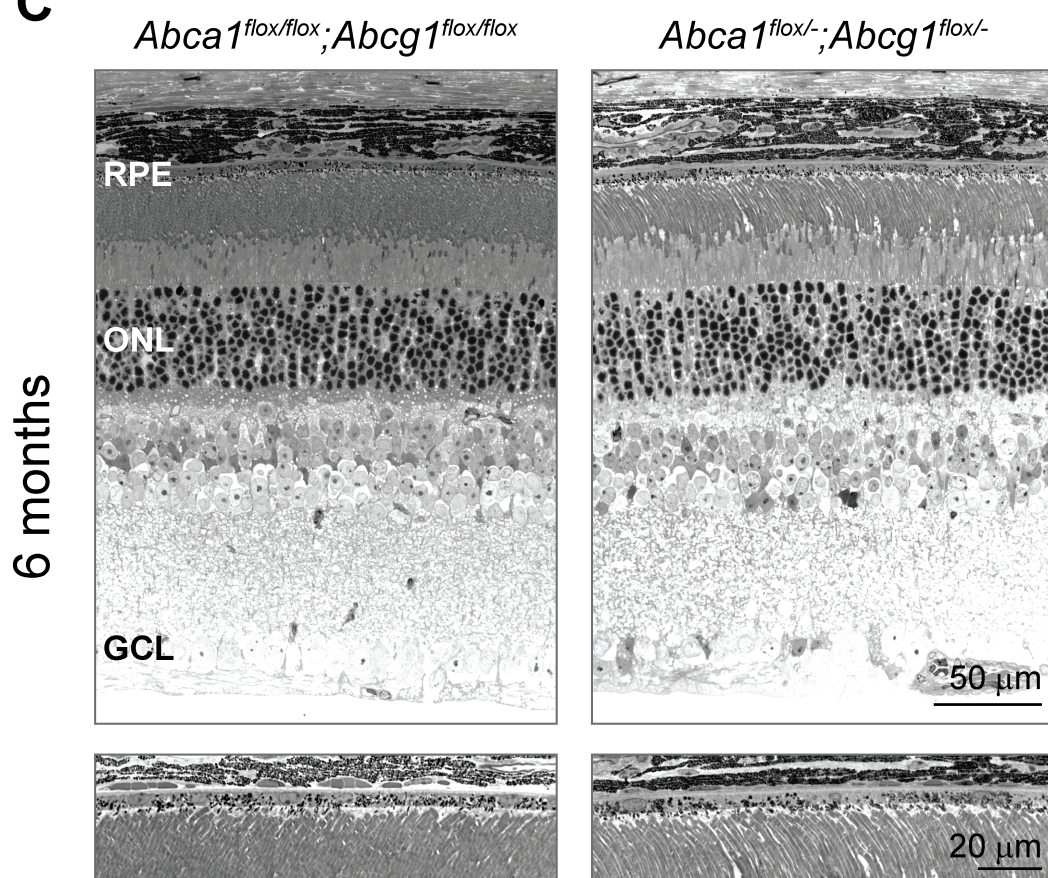


Figure 1 - Figure Supplement 2

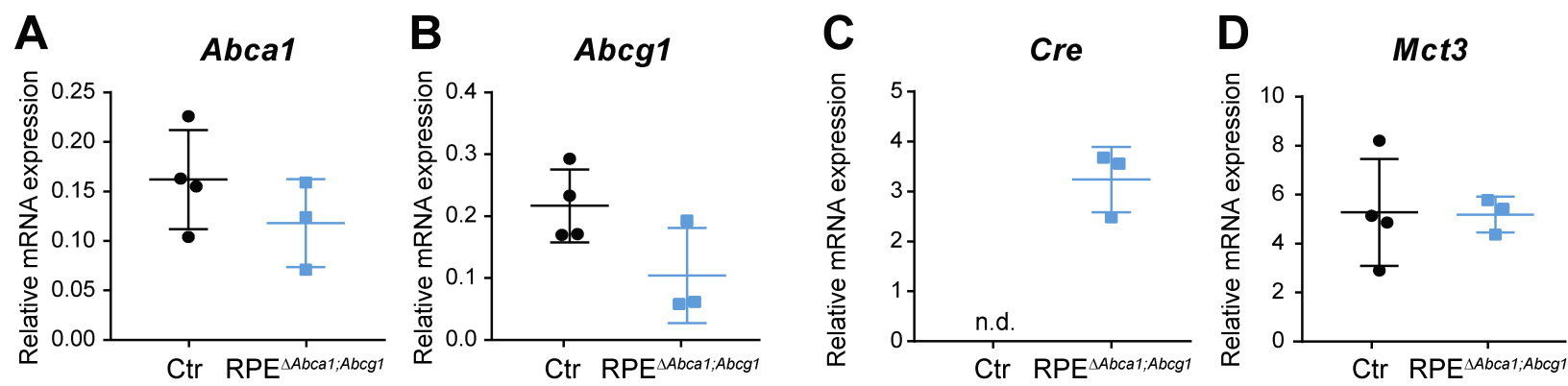


Figure 3 - Figure Supplement 1

Cre

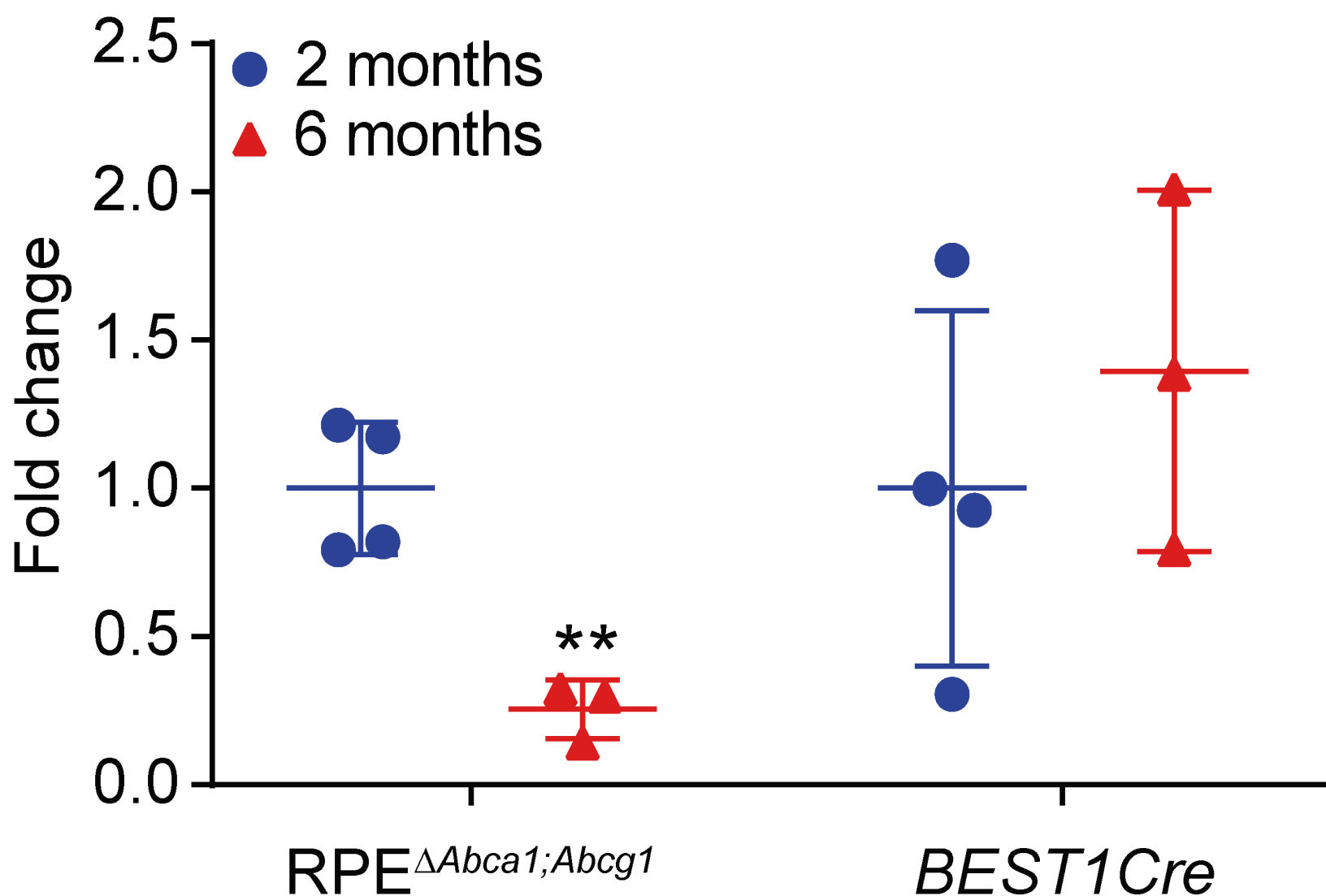


Figure 3 - Figure Supplement 2

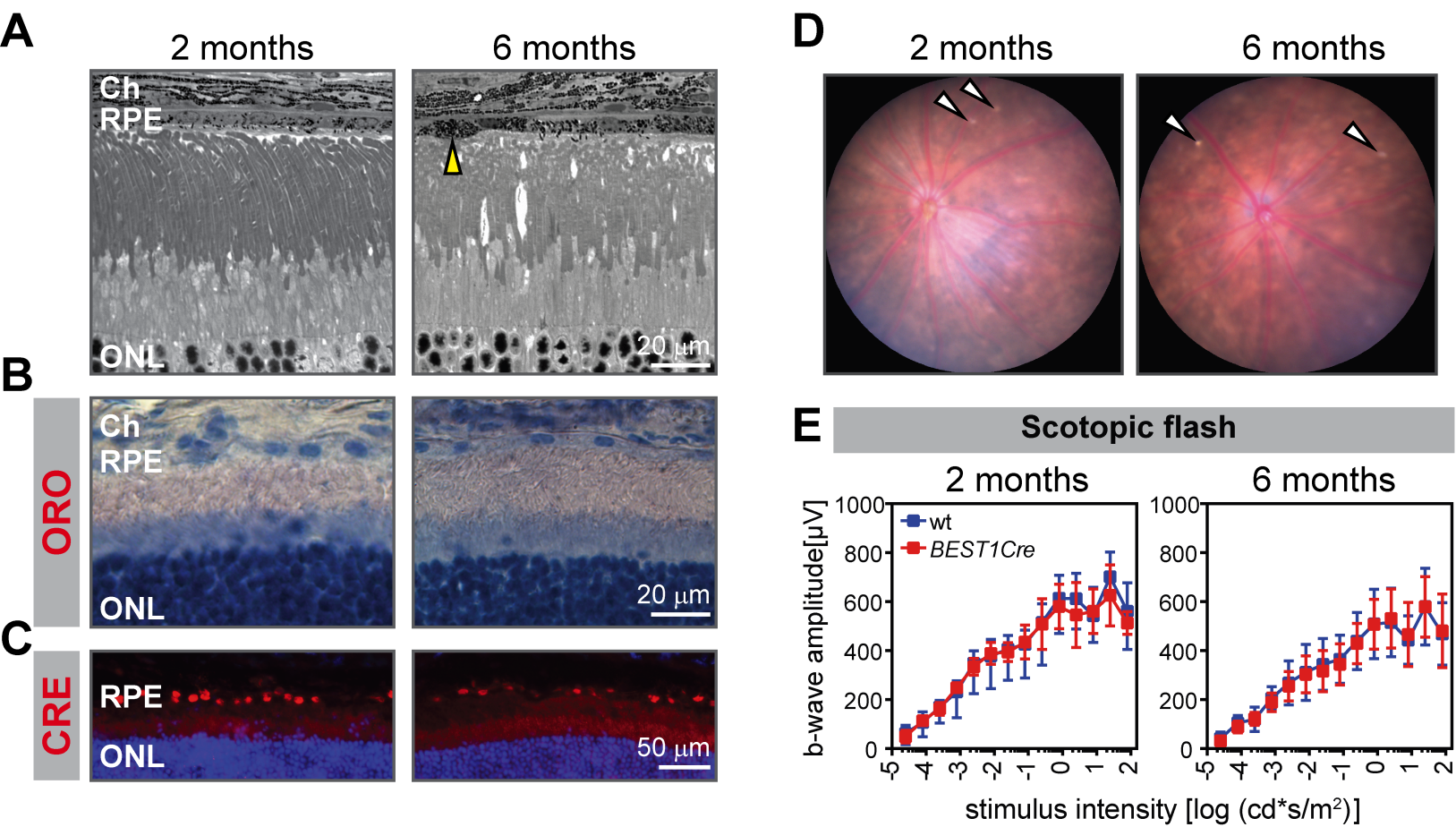
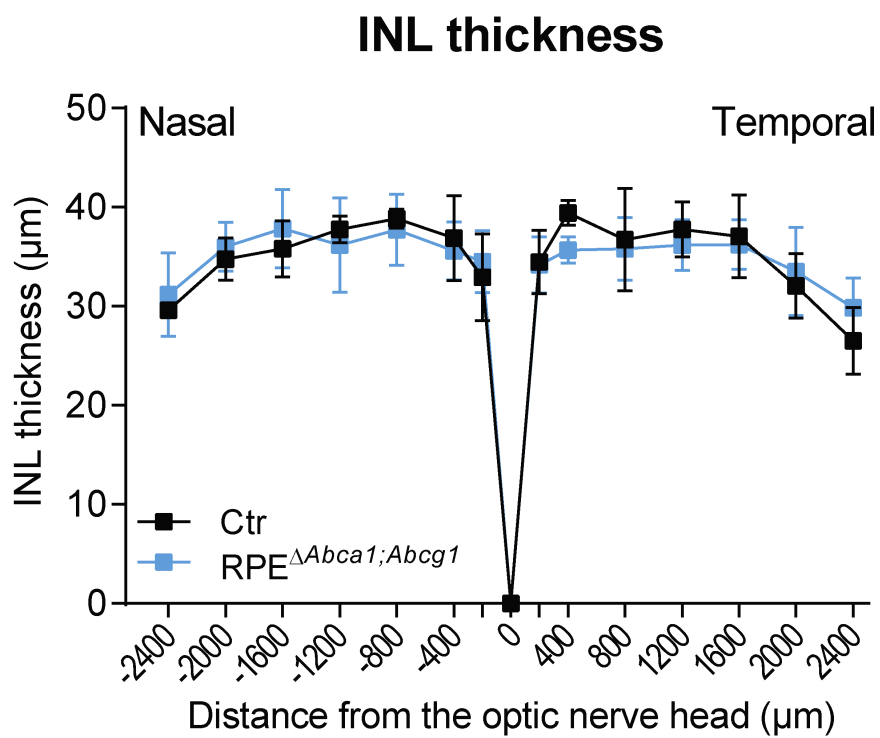


Figure 7 - Figure Supplement 1

A



B

